DYNAMIC ACTIVE FLOW CONTROL OF THE ROLL MOMENT ON A GENERIC UCAS WING

BY

XIAOWEI HE

Submitted in partial fulfillment of the
requirements for the degree of
Master of Science in Mechanical and Aerospace Engineering
in the Graduate College of the
Illinois Institute of Technology

Approved _____
Advisor

Chicago, Illinois
December 2017

ACKNOWLEDGMENT

I would like to give my deep gratitude to my advisor, Dr. David R. Williams, for his patient advisory and strong support throughout my study at IIT. I also would like to thank my lab mates, Xuanhong An, Muhammad Zubair Feroz, and Mathieu Le Provost, for their much help on many aspects of my research. Thanks also due to my former lab mate, Quentin Charbonnel, for his contribution to the preliminary design of the pitching and rolling mechanism.

I should thank my colleague in the FDRC, Katherine J. Asztalos, for her help on the flow visualization and other helpful discussions on my research. I also should thank my thesis committee members, Dr. Candace E. Wark and Dr. Seebany Datta-Barua, for their efforts on helping me complete this thesis. The Office of Naval Research has been supporting my research since the beginning of this project, I would not be able to pursue my degree without their support.

Last but not least, I would like to thank my parents and family, for their unreserved support and continuous faith in me over a long time and a long distance.

TABLE OF CONTENTS

Page

ACKNOWLEDGEMENT iii

LIST OF FIGURES ix

LIST OF SYMBOLS x

ABSTRACT xiii

CHAPTER

1. INTRODUCTION 1

2. EXPERIMENTAL SETUP 4

2.1. The Andrew Fejer Unsteady Wind Tunnel 4
2.2. ICE Wing Model 4
2.3. Roll and Pitch Maneuver Mechanism 8
2.4. Force and Moment Measurements 10
2.5. Surface Pressure Measurements 13
2.6. Active Flow Control Actuation 15

3. NON-CONTROLLED EXPERIMENTAL RESULTS 18

3.1. Physical Parameters 18
3.2. Steady Baselines 23
3.3. Dynamic Roll Measurements 27
3.4. Smoke Wire Flow Visualizaiton 42

4. ACTUATION TESTS 47

4.1. Static Maps 47
4.2. Dynamic Response 49
4.3. Control Authority on the Roll Moment 51

5. DESIGN OF THE CONTROL SYSTEM 53

5.1. Open-Loop Control System 53
5.2. Plant Model 55
5.3. Disturbance Model 58

5.4. Simulation Results 60

6. CONCLUSION 68

6.1. Summary of the Aerodynamic Force and Pressure Measurements 68
6.2. Summary of the Actuation Tests and Open-Loop Control System 69
6.3. Future Work 69

APPENDIX 70

A. TYPICAL PERFORMANCE OF CLIPPARD EVP PROPORTIONAL VALVES 71

B. LIFT AND DRAG COEFFICIENT MEASUREMENTS OF THE ICE WING MODEL BY THE UNITIED STATES AIR FORCE ACADEMY 73

BIBLIOGRAPHY 75

LIST OF FIGURES

Figure		Page
2.1	Airfoils and their locations with respect to the root chord	5
2.2	3-D profile of the wing and the body reference frame	5
2.3	The planform geometry (top view)	6
2.4	The shell and the supporting structures of the wing	7
2.5	The parts of the wing model	8
2.6	The roll maneuver mechanism	9
2.7	The pitching maneuver mechanism	10
2.8	Force and moment measurement coordinates	11
2.9	Positions the mac/4 and the force transducer	12
2.10	Pressure sensors on the upper wing	14
2.11	Pressure sensor locations (top view)	14
2.12	Inner structure of the actuator (top cross-section view)	16
2.13	Coanda effect on the actuator (side cross-section view)	17
2.14	The actuation control mechanism	17
3.1	Example profile of the effective angle of attack	22
3.2	Lift coefficient baseline measurement	23
3.3	Drag coefficient baseline measurement	24
3.4	Pitch moment coefficient baseline measurement	24
3.5	Pressure coefficient baselines	26
3.6	Roll moment coefficient of 0.5 Hz cases ($A = 30°$)	28
3.7	Roll moment coefficient of 1.0 Hz cases ($A = 30°$)	28
3.8	Roll moment coefficient of 1.5 Hz cases ($A = 30°$)	29
3.9	Roll moment coefficient of 2.0 Hz cases ($A = 30°$)	29
3.10	Roll moment coefficient amplitude vs. roll frequency ($A = 30°$)	30

3.11 Phase delay between the roll moment coefficients and the roll rates ($A = 30°$) 31

3.12 Time delay between the roll moment coefficients and the roll rates ($A = 30°$) 31

3.13 Roll moment coefficient of different roll amplitudes at 1.0 Hz (AOA = 0°) 33

3.14 Roll moment coefficient of different roll amplitudes at 2.0 Hz (AOA = 10°) 33

3.15 Pitch moment coefficient at 1.0 Hz (AOA = 0°) 35

3.16 Pitch moment coefficient at 1.0 Hz (AOA = 5°) 36

3.17 Pitch moment coefficient at 2.0 Hz (AOA = 5°) 36

3.18 Pitch moment coefficient at 2.0 Hz (AOA = 10°) 37

3.19 Pitch moment coefficient at 2.0 Hz (AOA = 5°) 37

3.20 Lift coefficient at 2.0 Hz (AOA = 0°) 39

3.21 Lift coefficient at 2.0 Hz (AOA = 5°) 39

3.22 Lift coefficient at 2.0 Hz (AOA = 20°) 40

3.23 Pressure coefficient measurements at 1.0 Hz (AOA = 5°) 41

3.24 Smoke wire visualization of the steady wing 43

3.25 Smoke wire visualization of the leading edge vortex at 10° angle of attack 43

3.26 Smoke wire visualization of the dynamic rolling at 1.5 Hz with positive angular velocity, 10° angle of attack 44

3.27 Smoke wire visualization of the dynamic rolling at 1.5 Hz with negative angular velocity, 10° angle of attack 46

4.1 Roll moment coefficient static map of the actuation 48

4.2 Pitch moment coefficient static map of the actuation 48

4.3 Roll moment coefficient response to dynamic actuation at 0° angle of attack 49

4.4 Roll moment coefficient response to dynamic actuation at 10° angle of attack 50

4.5 Roll moment coefficient response to dynamic actuation at 20° angle of attack 50

4.6 Control authority on roll moment coefficient at 1.0 Hz (AOA = 0°) 51

4.7 Control authority on roll moment coefficient at 2.0 Hz (AOA = 10°) 52

5.1 Block diagram of the control system for roll moment 53

5.2 Static map of the roll moment coefficient response to the input voltage 54

5.3 Sample of PRBS input and output signals and identified plant model output 56

5.4 Frequency responses of the identified models and the nominal model 56

5.5 Nominal model and the plant gain 57

5.6 Function of the plant model gain at $\alpha = 10°$ 57

5.7 Frequency response of the disturbance model at $\alpha = 0°$ 58

5.8 Frequency response of the disturbance model at $\alpha = 5°$ 59

5.9 Frequency response of the disturbance model at $\alpha = 10°$ 59

5.10 Frequency response of the disturbance model at $\alpha = 20°$ 60

5.11 Simulation result of the plant model at $\alpha = 0°$ 61

5.12 Simulation result of the plant model at $\alpha = 10°$ 61

5.13 Simulation result of the feedforward loop at $\alpha = 0°$ 62

5.14 Simulation result of the feedforward loop at $\alpha = 10°$ 63

5.15 Simulation result of the disturbance model at $\alpha = 0°$ 64

5.16 Simulation result of the disturbance model at $\alpha = 20°$ 64

5.17 Simulink® diagram of the open-loop controller 65

5.18 Simulation result of the open-loop controller with $C_{l_{ref}} = 0$ 66

5.19 Simulation result of the open-loop controller with $C_{l_{ref}} = 0.01$ . . 67

5.20 Simulation result of attenuation of the roll moment hysteresis loop 67

A.1 Mass flow rate lookup chart of Clippard EVP Proportional Valves 72

A.2 Typical performance of Clippard EVP Proportional Valves 72

B.1 Lift coefficient baseline of the ICE model 74
B.2 Drag coefficient baseline of the ICE model 74

LIST OF SYMBOLS

Symbol	Definition
A	roll amplitude
A_{jet}	outlet aera of the actuator
b	wing span
C_D	drag coefficient
C_L	lift coefficient
C_l	roll moment coefficient
$C_{l_{ref}}$	reference roll moment coefficient as the input of the control system
$C_{m_{\text{mac}/4}}$	pitch moment coefficient referenced to mac/4
C_μ	momentum coefficient
C_p	pressure coefficient
$\bar{\bar{c}}$	mean aerodynamic chord
c_r	root chord
c_y	chord length as a funtion of span-wise position
D	drag
F_A	axial force
F_N	normal force
$F_{x,y,z}$	measured forces
f	roll frequency
k	nondimensional frequency
L	lift

M_l	roll moment
M_m	pitch moment
M_n	yaw moment
p	pressure
p_∞	free stream static pressure
q_∞	free stream dynamic pressure
Re	Reynolds number
S	planform aera
s	half wing span; Laplas vaiable
$T_{x,y,z}$	measured torques
t_c	convective time
t^+	nondimensionlized time
$\bar{U}_\infty$	mean free stream velocity
V_{jet}	jet flow speed of the actuator
V_{act}	input voltage to the actuators
$x,\ y,\ z$	body reference frame coordinates
$x_{\text{mac}/4}$	x-coordiante of the quarter mean aerodynamic chord in the body reference frame
x_{trans}	x-coordinate of the transducer in the body reference frame
y_{mac}	y-coordinate of the mean aerodynamic chord in the body reference frame
y_s	smoke sheet distance from the root chord
α	nominal angle of attack

α_{eff}	effective angle of attack
Λ	leading edge sweep angle
ν	kinematic viscosity
ϕ	roll angle
ρ	air density

ABSTRACT

This thesis focuses on the roll moment on a generic highly-swept UCAS delta wing and the control of it through active flow control techniques. The lift, drag, roll moment, pitch moment, and pressure coefficients were measured for both steady state and dynamic roll cases. A pair of pneumatic trailing edge actuators were designed for the control of the aerodynamic roll moment. A set of smoke wire flow visualization was conducted to observe the flow separation and vortex generation on top of the wing. The quasi-steady and dynamic aerodynamic roll moment response to the actuation were measured. A disturbance model and a control response model were developed based on the measurements through linear approaches. The models were interpreted in the design of the open-loop control system for the roll moment. The open-loop controller fairly attenuated hysteresis loop of the aerodynamic roll moment. The capability of the model identification approaches were demonstrated, as well as the limitations thereof. The controllability of the actuation to the dynamic roll moment on the wing was examined.

CHAPTER 1
INTRODUCTION

With the drop on the operating cost and avoidance of the risk of losing pilots in conflicts [1], uses of uninhabited combat aerial systems or vehicles (UCASs/UCAVs) have been rising in recent years. UCAVs are able to perform high-g maneuver beyond the limitation of human pilots [2]. This character advances UCAVs with significant advantage in aerial combats. The increasing demand for UCAVs requires research and development about the aerodynamics on such aircraft. Particularly, since the UCAVs are used in more and more complicated missions in which the flight environments are mostly unsteady, the understanding of unsteady aerodynamics on these aircraft becomes vital to the safe operation and performance expansion of UCAVs. An example task with unsteady flow environments which a UCAV could encounter is to land on an aircraft carrier on the sea. When approaching the landing phase, the aircraft has low speed and high angle of attack. The unsteady flow due to the wake of the superstructure on the carrier, which is also known as the "burble effect" [3], can cause the aircraft to stall during landing. Another example of the unsteady aerodynamics dominating the performance of UCAVs is when the aircraft undergoes rapid (or high-g) maneuvers, the flow field surrounding the aircraft becomes highly unsteady [2].

This thesis mainly investigates the effects of dynamic roll motion on the roll moment on a generic delta wing, while other sorts of forces and moments are also addressed. The aerodynamics of delta wings has been systematically studied since the late 1950's [4]. Due to its large impact on the lift generation on the delta wings at high angle of attack, the formation and breakdown of the leading edge vortex has always been one of the most interested areas of researches about delta wings. Experimental studies on the vortical flows over delta wings in steady flow conditions were performed

by Payne et al [4] and Honkan and Andreopoulos [5] for low-speed conditions, and Donohoe and Bannink [6] for high-speed conditions. The existence of a secondary vortex structure near the surface of the delta wing, which has an opposite direction with respect to the primary vortex, was confirmed [5]. These studies suggested that the formation and breakdown of the leading edge vortex are highly related to the angle of attack as well as the sweep angle of the leading edge. The unsteady aerodynamic properties on rolling or pitching delta wings were also investigated through numerical methods and experimental approaches. Time lags between the roll moment coefficient and the roll motion were discovered in dynamic forced-roll simulations [7]. On the other hand, experiments show that the pitching motion or other dynamic motions of the delta wing cause hysteresis loops on the aerodynamic forces and moments as well [8, 9].

The numerical study on the dynamic rolling delta wing showed that the vortex moves inward when the wing rolls downward [10]. In addition, the researches performed by Gursul et al [11, 12, 13] suggested the existence of coherent structures on the wing, and showed that the leading edge vortices change in an antisymmetric pattern on the sides of a delta wing.

Active flow control theories and technology have been growing fast and are applied to control the flow separation in both steady and unsteady conditions. Active flow control techniques are found sufficient for dynamic 2-D pitching maneuvers [14] as well as for stall and roll control on a delta wing [15].

The objectives of this thesis are to investigate the roll moment response to the disturbance from roll rate on a UCAS delta wing, and to apply active flow control techniques to alleviate the influence of the disturbance on the roll moment. The design of the control system leads to the development of lower-order models for the roll moment to the disturbance as well as to the actuation. Linear approaches are used

for the identification of the plant and disturbance models [16] after the experimental measurements are documented. Based on the plant model, a feedforward loop that prescribes the input to the plant is added to the open-loop controller [17].

In this thesis, Chapter 2 illustrates the design of the wing and the actuators, experimental setup, and the method of measuring forces and pressure. In Chapter 3, the primary physical parameters that are used in the experiments are given. This chapter then gives the experimental results of static measurements and dynamic measurements of the aerodynamic forces, moments and surface pressure. At the end of Chapter 3, the smoke wire flow visualization over the wing is provided. Chapter 4 shows the measurements of quasi-steady actuation dynamic actuation. The control authority of the actuation is also determined in this chapter. Chapter 5 discusses about the open-loop control system and the identification process of the plant model and the disturbance model. Simulation results of the open-loop controller are demonstrated in this chapter. At the end, in addition to the summary on the experiments and the control system, an outlook of future work is discussed in Chapter 6.

CHAPTER 2

EXPERIMENTAL SETUP

2.1 The Andrew Fejer Unsteady Wind Tunnel

The experiments of this thesis are conducted in the Andrew Fejer unsteady wind tunnel at IIT. The tunnel is a close-loop wind tunnel with a 2.1 m long test section. The cross-section dimensions of the test section is 0.61 m $\times$ 0.61 m. The flow runs from the left to the right through the test section. A set of shutter mechanism is instrumented at the downstream end of the test section, which can make the flow speed vary to create unsteady flows.

The test model is placed in the middle of the test section with nose pointing at the upstream direction. A pitot tube measures the free stream flow speed at the upstream end of the test section. The wind tunnel runs at fixed mean flow speed of $\bar{U}_\infty = 6.5$ m/s for all of the experiments of the thesis.

2.2 ICE Wing Model

2.2.1 Wing Geometry. This thesis uses a delta wing model which is based on the Lockheed Martin ICE-101 planform and the SACCON configuration profile. The root chord length is $c_r = 330$ mm and the wing span is $b = 287$ mm. The 3-D profile of the wing is constructed based on three airfoils (shown in Figure 2.1) that locate at the root, $1/3s$, and $2/3s$ from the root respectively, where $s = b/2$ is the half wing span. Along with the tips of the wing, a tailless delta wing is built as the profile of the physical wing model as shown in Figure 2.2.

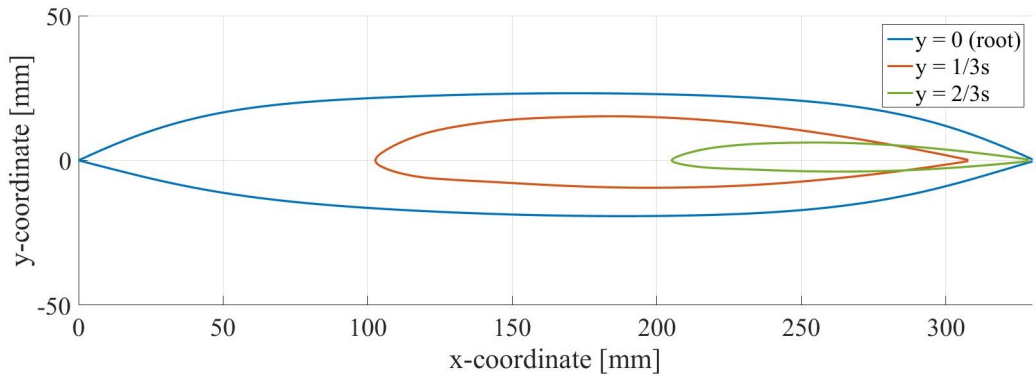

Figure 2.1. Airfoils and their locations with respect to the root chord

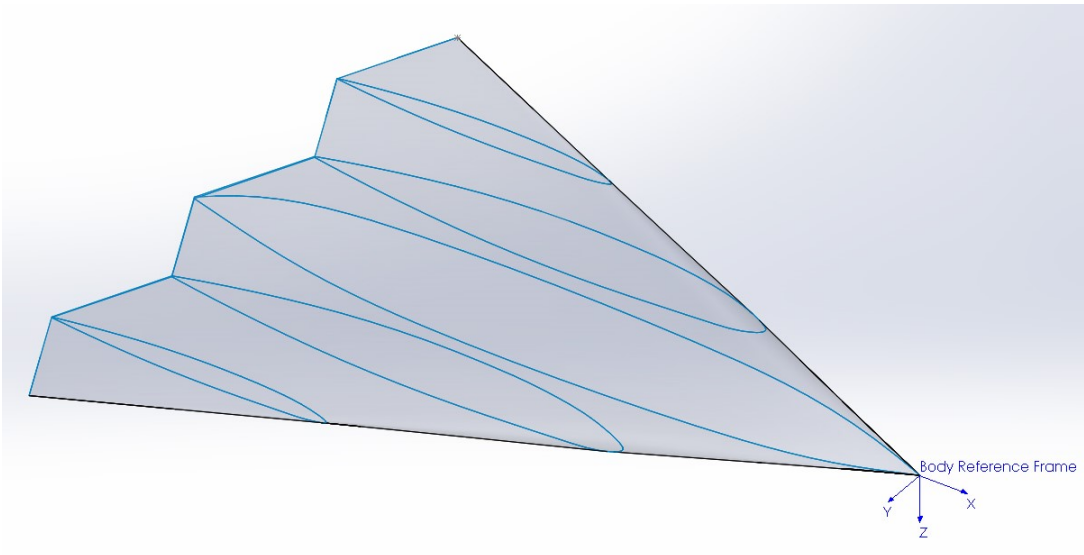

Figure 2.2. 3-D profile of the wing and the body reference frame

In this thesis, the body reference frame on the wing is orientated at the nose of the model, which is also shown in Figure 2.2. Figure 2.3 shows the top view of the planform. On this planform, the leading edge sweep angle Λ is 65 degrees. The planform area is calculated as: $S = 0.0474$ m^2. Given the planform geometry, the

mean aerodynamic chord is calculated by:

$$\bar{\bar{c}} = \frac{\int_0^s c_y^2 dy}{\int_0^s c_y dy}$$
$$c_y = \begin{cases} \dfrac{-3c_r + 2s\tan\Lambda}{s} y + c_r, \ 0 \leqslant y \leqslant \dfrac{1}{3}s \\ \dfrac{3c_r - 2s\tan\Lambda}{s} y - c_r + 2s\tan\Lambda, \ \dfrac{1}{3}s < y \leqslant \dfrac{2}{3}s \\ \dfrac{-3c_r + 2s\tan\Lambda}{s} y + 4c_r - 2s\tan\Lambda, \ \dfrac{2}{3}s < y \leqslant s \end{cases} \tag{2.1}$$

from which the mean aerodynamic chord is calculated as $\bar{\bar{c}} = 213.85$ mm. The position of the mean aerodynamic chord on the span direction is found as: $y_{\text{mac}} = 44.51$ mm, which is $0.31s$ from the root. Subsequently, the longitudinal coordinate of the quarter mean aerodynamic chord is found as: $x_{\text{mac}/4} = 148.91$ mm, which is $0.45c_r$ from the nose.

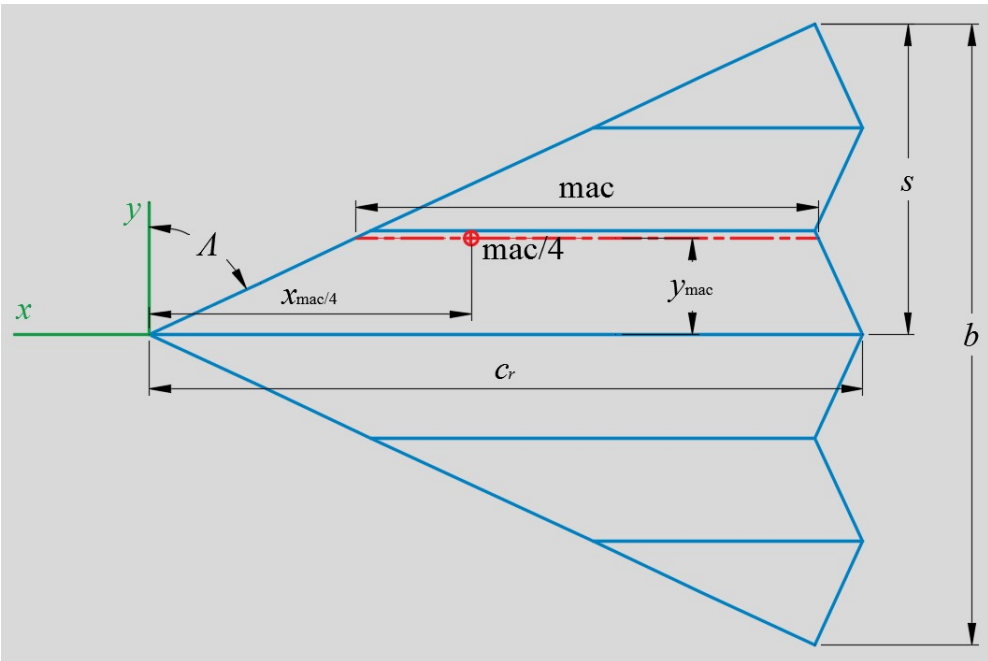

Figure 2.3. The planform geometry (top view)

2.2.2 Physical Model Structures. For the purpose of placing the supporting and moving mechanism, as well as the force transducer and the pressure sensors, the

interior of the model is made hollow. The profile of the wing is maintained through the shell of the model, which matches the 3-D profile that is given above. On the inner surface of the shell, 9 longitudinal frames and 6 lateral ribs are merged onto the shell, in order to provide the model of sustainable strength and stiffness. These design facts are shown in Figure 2.4.

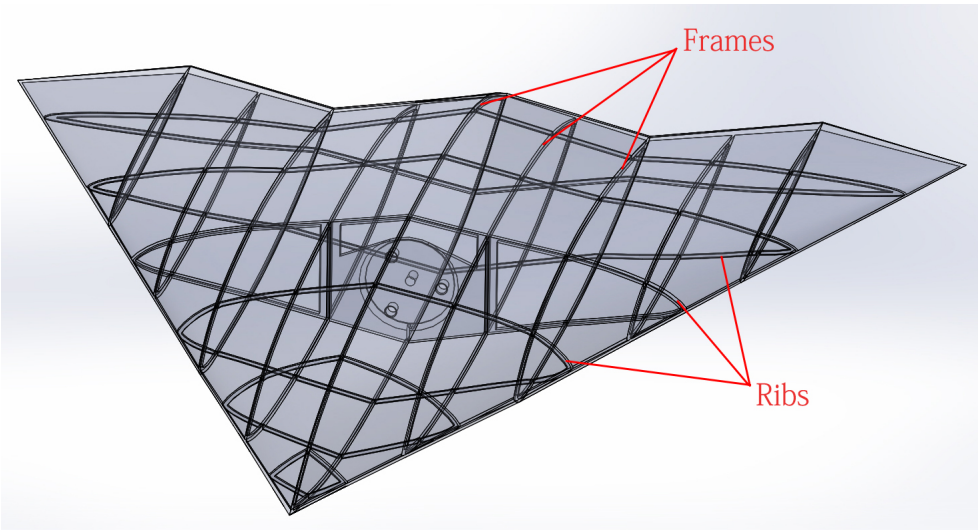

Figure 2.4. The shell and the supporting structures of the wing

The model is separated into two parts, so that it allows the mounting of the roll maneuver mechanism (discussed in Section 2.3.1) and the instrumenting of the force transducer (discussed in Section 2.4.1) and the pressure sensors (discussed in Section 2.5.1). While the top part of the wing is fixed onto the bottom part through thread fastening, the tip parts of the trailing edge are separated from the main wing to be further fabricated as the actuator modules (discussed in Section 2.6.1). The 3-D CAD model of these structures is demonstrated in Figure 2.5

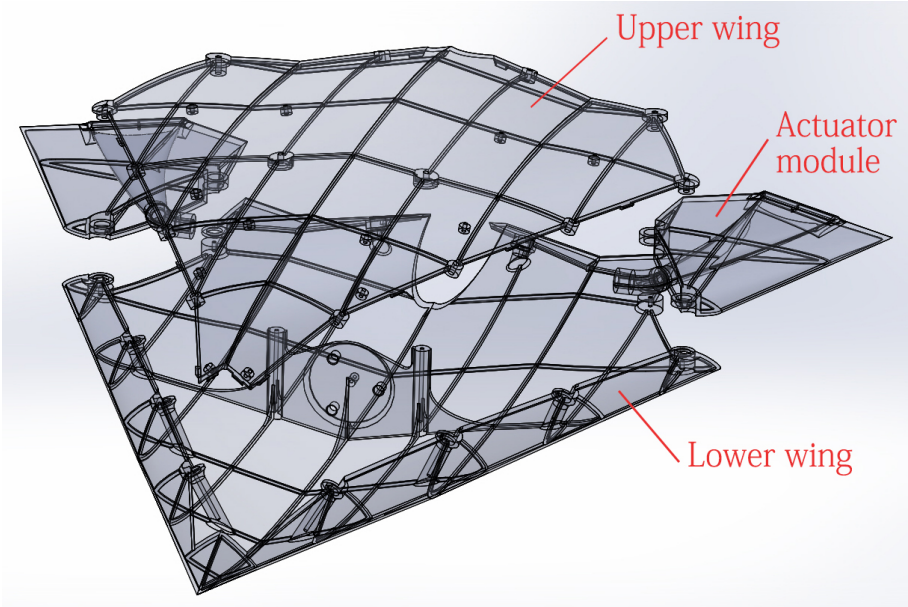

Figure 2.5. The parts of the wing model

2.3 Roll and Pitch Maneuver Mechanism

2.3.1 Roll Maneuver Mechanism. The roll motion of the model is realized by an HSB-9360TH servo motor which is placed behind the trailing edge of the wing. The servo connects the model through a hollow metal probe which is aligned with the root chord of the wing.

The servo is controlled by a 5 Volts pulse width modulated (PWM) signal at 50 Hz frequency. Depending on the length of the duty cycle of the PWM signal, the servo rotates within $\pm 90°$ with a highest roll rate at 17.44 rad/s (2.78 Hz). In addition, the roll angle measurement is extracted from the inner potentiometer of the servo as the instantaneous position feedback to the experiments. The roll maneuver mechanism is shown in Figure 2.6.

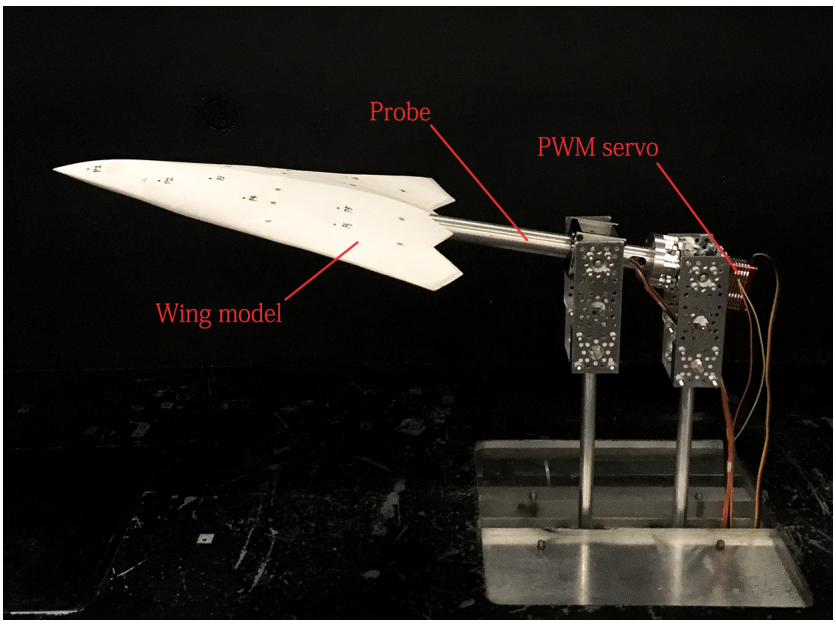

Figure 2.6. The roll maneuver mechanism

2.3.2 Pitch Maneuver Mechanism. A sleeve bar mechanism is used to carry out the pitch maneuver of the model, as shown in Figure 2.7. The linear bearing on the longitudinal probe along with the hinges convert the height differential between the two vertical rods into the various angles of attack of the wing. A pair of linear servos control the vertical position of the two rods individually, so that they make the model pitch and/or plunge instantaneously or maintain a certain angle of attack depending on the needs of the experiments.

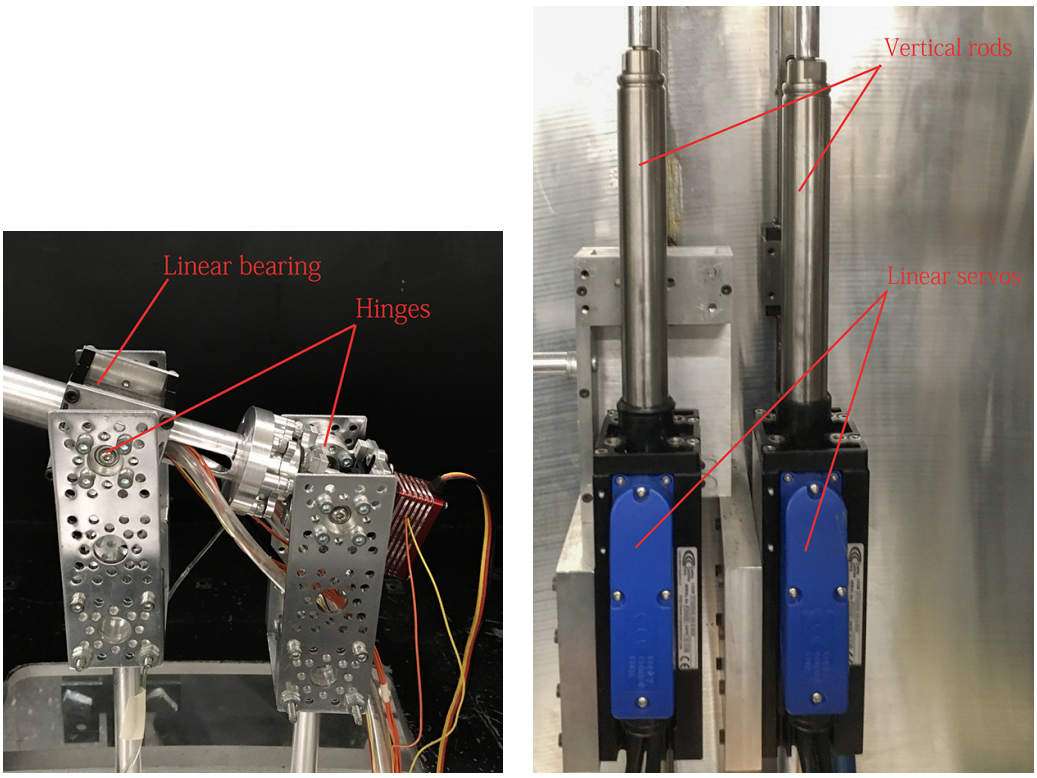

(a) Linear bearing and hinges (b) Vertical rods and linear servos

Figure 2.7. The pitching maneuver mechanism

2.4 Force and Moment Measurements

2.4.1 Force Transducer. An ATI Nano 25 force balance transducer is used to measure the forces and moments in the experiments. The force transducer can measure the forces and moments on three axes simultaneously, which enables the real-time measuring of the normal and axial forces, as well as the roll, pitch, and yaw moments. The measurement coordinate system is aligned with the body reference frame, which is demonstrated in Figure 2.8. In the longitudinal direction, the transducer is located at $x_{\text{trans}} = \frac{7}{24} b \tan \Lambda$ on the x-axis, which gives $x_{\text{trans}} = 179.52$ mm $(0.54c_r)$ from the nose. Comparing with the quarter mean aerodynamic chord position, the transducer is located $0.09c_r$ downstream of the mac/4.

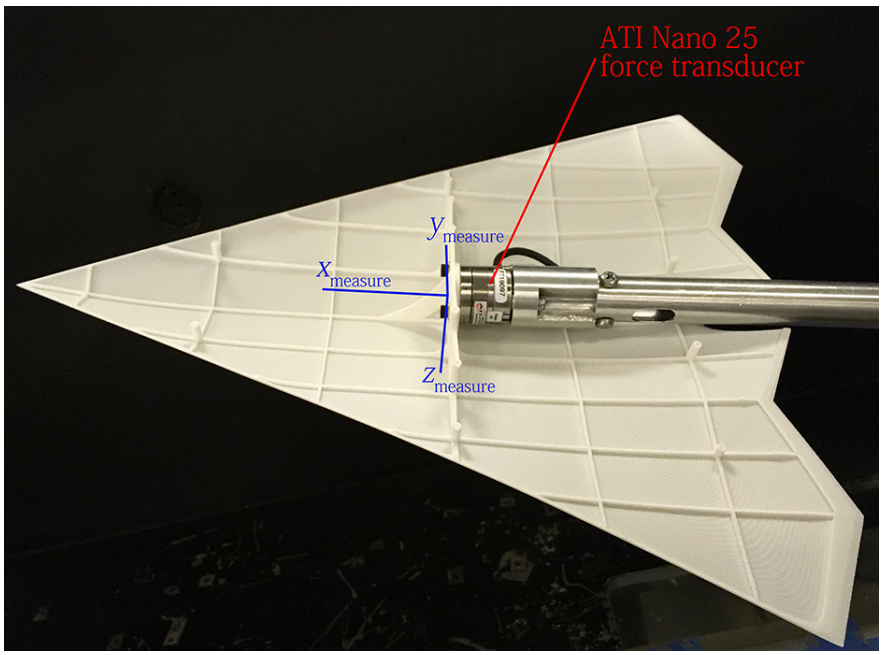

Figure 2.8. Force and moment measurement coordinates

2.4.2 Adjustment of the Force and Moment Measurements. A dual-offset process is implemented to all of the measurements in order to eliminate the drift of the transducer and to compensate for the additional y-moment due to the moment arm between the center of gravity and the transducer as shown in Figure 2.9.

The offset of the force transducer drifts on a larger time scale than the duration of each experiment session. This may cause the force and moment measurements to be less accurate than they are supposed to be. Therefore, a tare of the offset is used by taking offsets before each experiment session and afterward independently, so that the drift of the transducer is compensated by taking the average offset value of the before and after offsets.

The location of $x_{\text{mac}/4}$ is the reference point for the calculation of the pitch and yaw moments. For the pitch moment, the corrected measurement is obtained as:

$$M_{m_{\text{mac}/4}} = T_y + F_z(x_{\text{trans}} - x_{\text{mac}/4}) \tag{2.2}$$

where T_y is the torque measurement on y-axis, and F_z is the force measurement on z-axis.

Similarly, the corrected yaw moment measurement is calculated as,

$$M_{n_{\mathrm{mac}/4=}} = T_z - F_y(x_{\mathrm{trans}} - x_{\mathrm{mac}/4}) \tag{2.3}$$

where T_z is the torque measurement on z-axis, and F_y is the force measurement on y-axis.

In the remainder of this thesis, if it is not specified, the pitch moment M_l and yaw moment M_n are the moments about the quarter mean aerodynamic chord, $M_{m_{\mathrm{mac}/4}}$ and $M_{n_{\mathrm{mac}/4}}$ respectively.

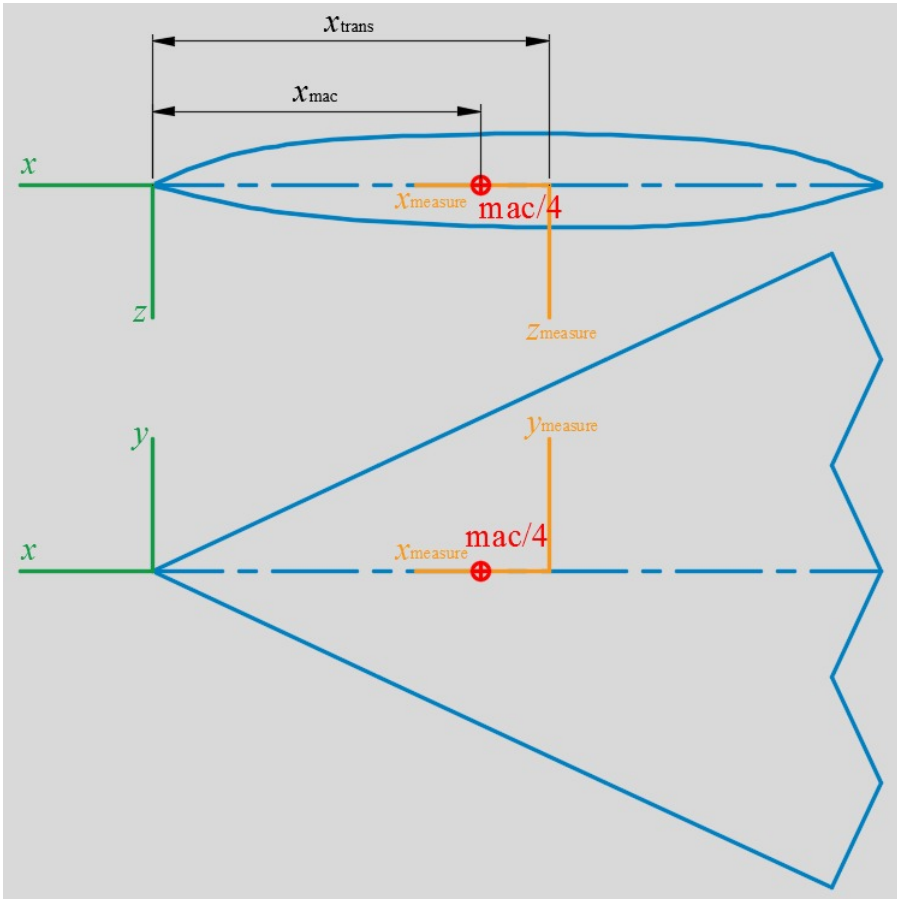

Figure 2.9. Positions the mac/4 and the force transducer

2.4.3 Aerodynamic Forces and Moments. When the model is rolling in an experiment session, the instantaneous force and moment measurements on the force transducer are the sum of the inertia of the model, the added mass effect (which is the inertia of the air), and the forces and moments due to aerodynamics, which are written as:

$$\begin{aligned} \boldsymbol{F}_{\text{total}} &= \boldsymbol{F}_{\text{inertia}} + \boldsymbol{F}_{\text{add}} + \boldsymbol{F}_{\text{aero}} \\ \boldsymbol{M}_{\text{total}} &= \boldsymbol{M}_{\text{inertia}} + \boldsymbol{M}_{\text{add}} + \boldsymbol{M}_{\text{aero}} \end{aligned} \tag{2.4}$$

While the flow-on cases (in which the tunnel is running at $\bar{U}_\infty$) measure the $\boldsymbol{F}_{\text{total}}$ and $\boldsymbol{M}_{\text{total}}$, the $\boldsymbol{F}_{\text{inertia}} + \boldsymbol{F}_{\text{add}}$ and $\boldsymbol{M}_{\text{inertia}} + \boldsymbol{M}_{\text{add}}$ are measured in the flow-off cases (in which the tunnel is not running, thus there is no free stream). The aerodynamic forces and moments are obtained by subtracting the measurements of the flow-off cases from the corresponding ones of the flow-on cases, as shown in Equation 2.5, such that the remaining parts are considered to be irrelevant to the inertia and added mass effect, and is solely due to the aerodynamics.

$$\begin{aligned} \boldsymbol{F}_{\text{aero}} &= \boldsymbol{F}_{\text{flow-on}} - \boldsymbol{F}_{\text{flow-off}} \\ \boldsymbol{M}_{\text{aero}} &= \boldsymbol{M}_{\text{flow-on}} - \boldsymbol{M}_{\text{flow-off}} \end{aligned} \tag{2.5}$$

This assumes that the "added mass" is measured correctly in the flow-off case.

2.5 Surface Pressure Measurements

2.5.1 Pressure Sensors and Measurement Locations. Twelve All Sensor 1 INCH-D2-4V-MINI pressure differential sensors are symmetrically distributed about the root chord on the upper surface of the wing model to measure the surface pressure, as shown in Figure 2.10. The sensors are labeled as P1, P2, ..., P6 for those on the port side of the wing, and S1, S2, ..., S6 for those on the starboard side, as shown in Figure 2.11. Such configuration of sensor location is able to measure both then inboard (odd-number sensors) and the outboard (even-number sensors) surface pressure on the wing.

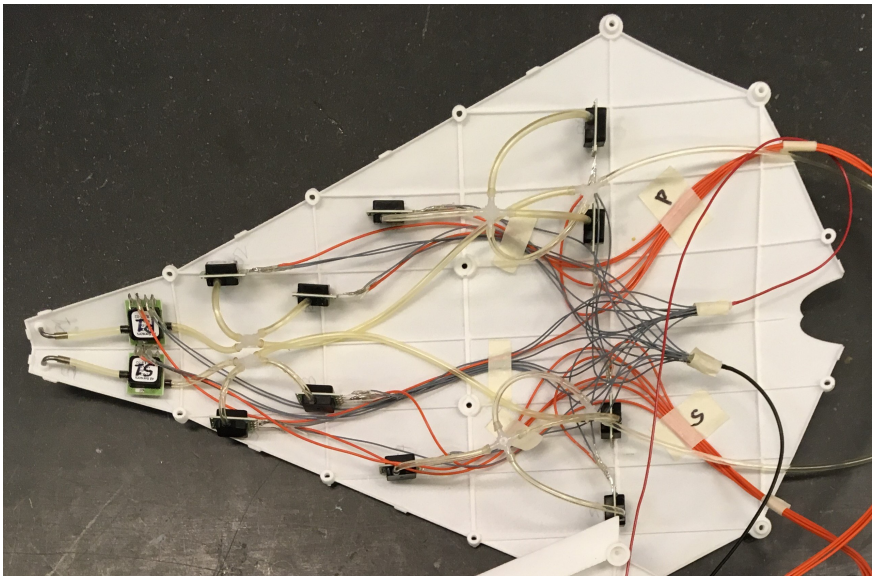

Figure 2.10. Pressure sensors on the upper wing

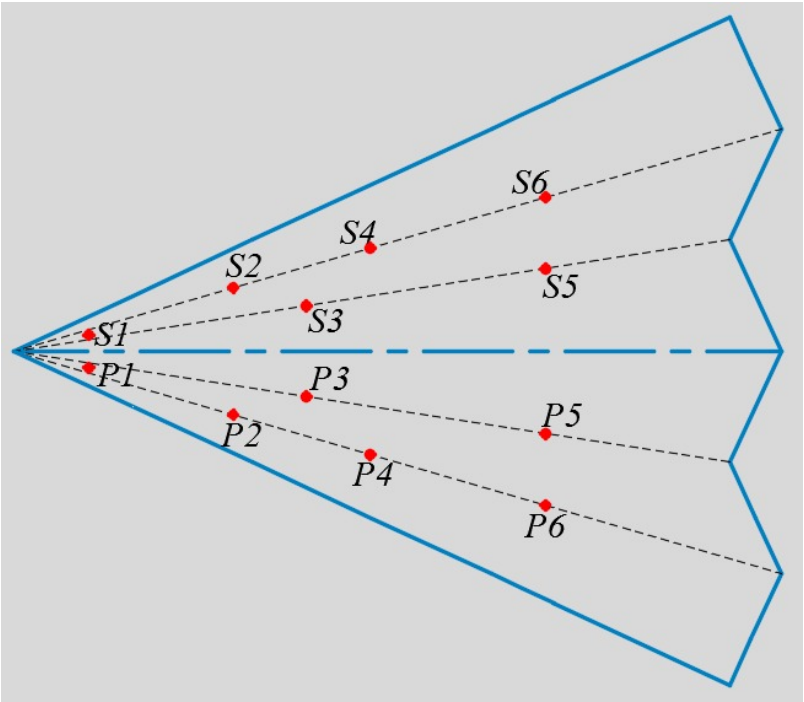

Figure 2.11. Pressure sensor locations (top view)

2.5.2 Aerodynamic Pressure. Similar to the force and moment measurements, the pressure differential due to aerodynamics is obtained by subtracting the flow-off measurements from the flow-on measurements. All of the pressure sensors share a common pressure reference, which is the free stream static pressure. Therefore the pressure measurement directly gives $p - p_\infty$, for the calculation of pressure coefficient:

$$C_p = \frac{p - p_\infty}{q_\infty} \tag{2.6}$$

Thus,

$$C_{p_{\text{aero}}} = C_{p_{\text{flow-on}}} - C_{p_{\text{flow-off}}} \tag{2.7}$$

2.6 Active Flow Control Actuation

2.6.1 Trailing Edge Actuators. Two symmetric actuators for flow control are made based on the tip parts on the trailing edge of the model, as shown in Figure 2.5. Each actuator has a curved volume which compresses the air from the pipe to a uniform jet flow at the outlet. The outlet is made by a cylinder and a slot. The length of the slot is $l_{\text{slot}} = 30$ mm and the width $w_{\text{slot}} = 0.2$ mm, which is 1/10 of the diameter of the cylinder. When the jet flow comes out from the slot, the Coanda effect bends the flow downward. The detailed structure of the actuator is specified in Figure 2.12 and Figure 2.13.

2.6.2 Control of the Actuation. The strength of actuation is measured by the momentum coefficient C_μ, which is calculated by:

$$C_\mu = \frac{\rho V_{\text{jet}}^2 A_{\text{jet}}}{q_\infty S} \tag{2.8}$$

where ρ is the air density, V_{jet} is the speed of the jet flow that comes out from the slot of the actuator, $A_{\text{jet}} = l_{\text{slot}} w_{\text{slot}} = 6 \times 10^{-6}$ m^2, q_∞ is the dynamic pressure of the free steam, and S is the planform area of the wing.

A pair of Clippard EV-P-10-4050 proportional valves is used to regulate the

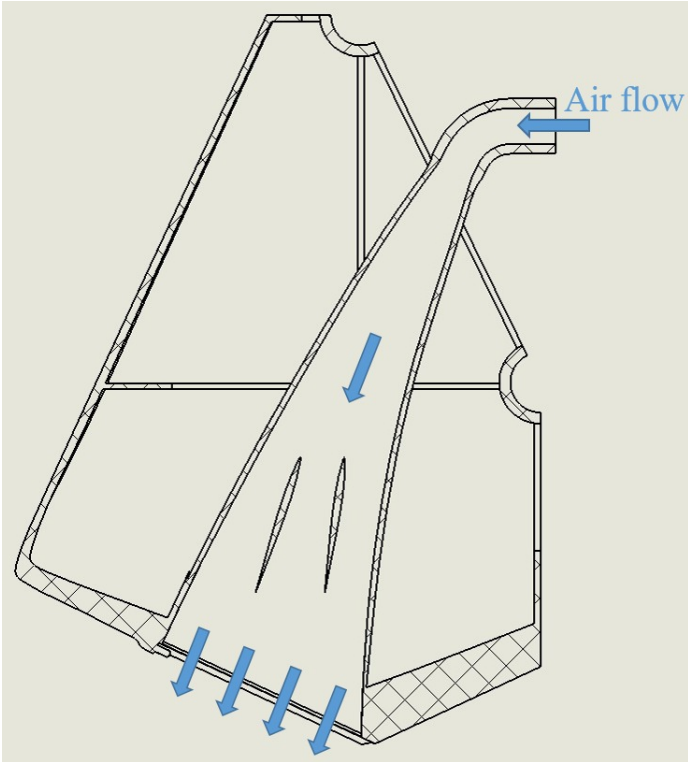

Figure 2.12. Inner structure of the actuator (top cross-section view)

mass flow rate in the pipes, thus controlling the C_μ for each actuator individually. When a constant 35 psi pressure is provided at the inlet of the valve, the volume flow rate Q_{jet} varies from 0 to $2.33 \times 10^{-}5$ m^3/s (see Appendix A), depending on the control voltage which varies from 0 to 10 V correspondingly. Therefore, the V_{jet} term in Equation 2.8 can be calculated by:

$$V_{\text{jet}} = \frac{Q_{\text{jet}}}{A_{\text{jet}}} \tag{2.9}$$

With an average free stream speed $\bar{U}_\infty = 6.5$ m/s, the maximum momentum coefficient that a single actuator gives is 0.009.

As shown in Figure 2.14, the actuator control mechanism is made up by the pressure source, the pressure gauge, and the proportional valve. The valve is connected with the control board which converts the analog voltage signal to current single for the valve.

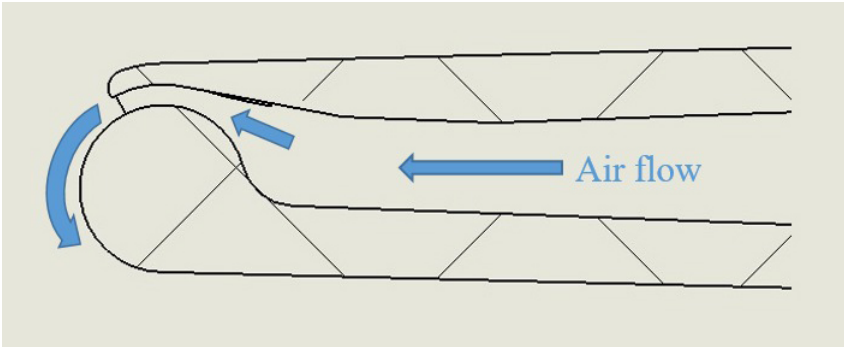

Figure 2.13. Coanda effect on the actuator (side cross-section view)

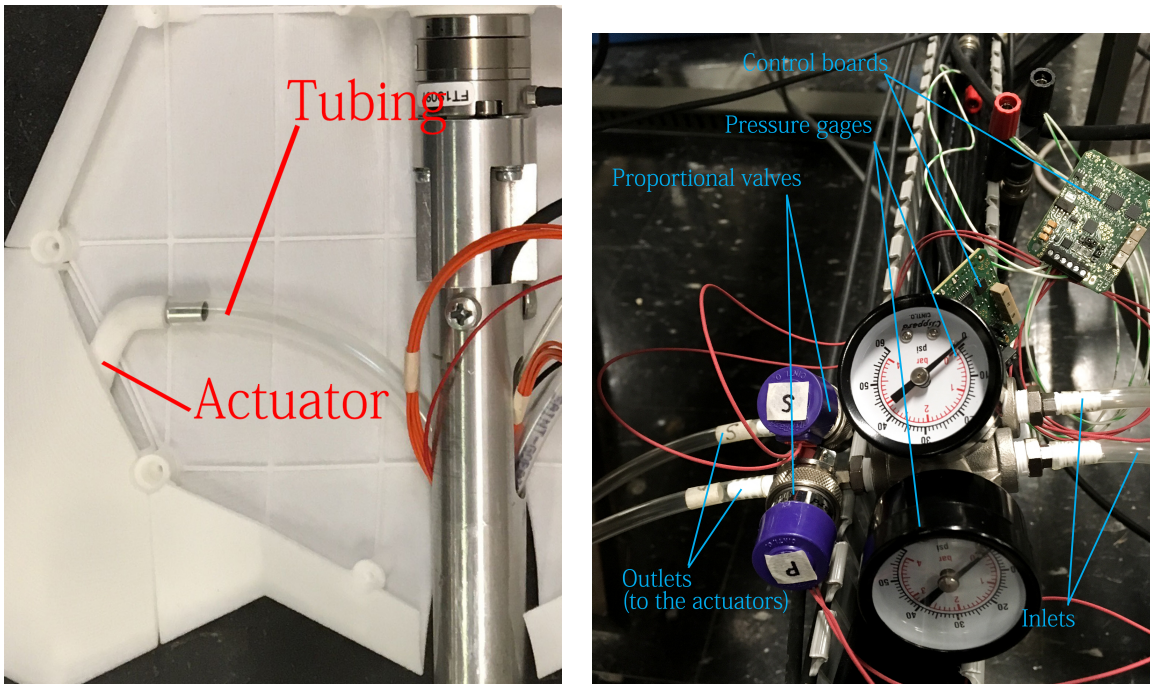

(a) Inlet of the actuator

(b) Actuation control hardware

Figure 2.14. The actuation control mechanism

CHAPTER 3

NON-CONTROLLED EXPERIMENTAL RESULTS

This chapter gives the measurements of the aerodynamic forces and moments, as well as the pressure coefficients from the experiments in which the wing rolls dynamically without any actuation. Therefore, these measurements provide the force and moment response to the dynamic roll disturbance on the wing.

Section 3.1 first gives the important physical parameters of the experiments. Then, the steady state lift, drag, pitch moment, and pressure coefficients are shown in Section 3.2. Section 3.3 analyze the dynamic response of the roll moment, pitch moment, and lift coefficients to the roll motion. At the end of this chapter, Section 3.4 demonstrate some sets of smoke wire flow visualization over the wing.

3.1 Physical Parameters

3.1.1 Reynolds Number. All experiments are conducted in the Andrew Fejer Unsteady Wind Tunnel at IIT with a mean flow velocity of $\bar{U}_\infty = 6.5$ m/s. Using the mean aerodynamic chord as the longitudinal length reference, the Reynolds number is obtained as:

$$\mathrm{Re} = \frac{\bar{U}_\infty \bar{\bar{c}}}{\nu} \tag{3.1}$$

where $\bar{U}_\infty = 6.5$ m/s, $\nu = 1.451 \times 10^{-5}$ m^2/s, and $\bar{\bar{c}} = 213.85 \times 10^{-3}$ m as calculated in Equation 2.1. Given these parameters, the Reynolds number referenced to the mean aerodynamic chord of the experiments is: $\mathrm{Re} = 9.5677 \times 10^4$.

3.1.2 Nondimensional Roll Frequency. The nondimensional frequency, or reduced frequency, is a dimensionless parameter that describes the unsteadiness of the flow, which is calculated as [18]:

$$k = \frac{\omega \frac{c}{2}}{\bar{U}_\infty} \tag{3.2}$$

where ω is the circular frequency and c is the chord length. For a pitching 2-D airfoil, the semi-chord is used as the length scale as it is in Equation 3.2. Though the unsteadiness of the flow over the wing is due to the roll motion of the 3-D wing in this thesis, the wing encounters the unsteadiness mainly through the change of the effective angle of attack, which has a similar mechanism to a pitching airfoil, except that the reference length scale is the mean aerodynamic chord. Thus, Equation 3.2 becomes:

$$k = \frac{\omega \frac{\bar{\bar{c}}}{2}}{\bar{U}_\infty} = \frac{\pi f \bar{\bar{c}}}{\bar{U}_\infty} \tag{3.3}$$

where f is the roll frequency of the wing and $\bar{\bar{c}}$ is the mean aerodynamic chord length.

In this thesis, the roll frequencies of the wing are $f = 0.5$ Hz, 1.0 Hz, 1.5 Hz, and 2.0 Hz. Given the $\bar{U}_\infty$ and the $\bar{\bar{c}}$ value, the corresponding reduced frequencies are $k = 0.0516$, 0.1033, 0.1550, and 0.2066 respectively.

3.1.3 Effective Angle of Attack. The effective angle of attack in the experiments is a superposition of two parts. One is the quasi-steady angle of attack due to the roll angle, another part is the induced angle of attack due to the roll rate:

$$\alpha_{\text{eff}} = \alpha_{\text{qs}} + \alpha_{\text{in}} \tag{3.4}$$

The quasi-steady angle of attack is determined by the nominal angle of attack and the instantaneous roll angle. The body reference frame at zero nominal angle of attack with zero roll and angle ($\alpha = 0$, $\phi = 0$) is considered as the initial body reference frame: $\boldsymbol{B_i}$. The free steam velocity in the initial body reference frame can be written as:

$$\boldsymbol{U}_{/B_i} = [1 \;\; 0 \;\; 0]^{\mathrm{T}} \tag{3.5}$$

At a certain nominal angle of attack α, the wing (and thus the body reference frame) rolls about the root chord, which is the x-axis of the intermediate reference frame $\boldsymbol{B_{im}}$. Therefore, when the wing is at an angle of attack and a roll angle, the instantaneous

body reference frame is the rotated body reference frame $\boldsymbol{B_r}$, which has rotated about the y-axis of $\boldsymbol{B_i}$ by α degrees and then rotated about the x-axis of $\boldsymbol{B_{im}}$ by ϕ degrees. The unit vector of the z-axis in the rotated body reference frame is:

$$\boldsymbol{n}_{/B_r} = [0 \;\; 0 \;\; 1]^{\mathrm{T}} \tag{3.6}$$

Applying the linear transformation of coordinate systems [19], the free steam velocity in the rotated body reference frame is:

$$\boldsymbol{U}_{/B_r} = [\cos\alpha \quad \sin\phi\cos\alpha \quad \cos\phi\sin\alpha]^{\mathrm{T}} \tag{3.7}$$

Thus, we obtain the quasi-steady angle of attack:

$$\begin{aligned} \alpha_{\mathrm{qs}} &= 90^\circ - \cos^{-1}(\boldsymbol{U}_{/B_r} \cdot \boldsymbol{n}_{/B_r}) \\ \alpha_{\mathrm{qs}} &= 90^\circ - \cos^{-1}(\cos\phi\sin\alpha) \end{aligned} \tag{3.8}$$

The roll rate induced angle of attack is determined by the roll rate itself, which leads to the induced normal velocity on the wing. The induced velocity varies as the distance between the measurement location and the roll axis, which is the x-axis of the body reference frame, and it changes throughout the wing span. To keep the same reference scale with other derivations and calculations, the induced angle of attack is calculated at the mean aerodynamic chord, which has a distance to the root chord of $y_{\mathrm{mac}} = 44.51$ mm as shown in Section 2.2.1. Thus, the induced angle of attack is obtained as:

$$\alpha_{in} = \tan^{-1} \frac{\cos\alpha}{\dfrac{\bar{U}_\infty}{U_{in}} + \sin\alpha} \tag{3.9}$$

where U_{in} is the induced velocity:

$$U_{in} = \omega(t) y_{\mathrm{mac}} = \dot{\phi}(t) y_{\mathrm{mac}} \tag{3.10}$$

Substituting Equation 3.8 and Equation 3.9 into Equation 3.4, the effective

angle of attack is:

$$\alpha_{\text{eff}} = 90^\circ - \cos^{-1}(\cos\phi \sin\alpha) + \tan^{-1} \frac{\cos\alpha}{\dfrac{\bar{U}_\infty}{\dot{\phi} y_{\text{mac}}} + \sin\alpha} \tag{3.11}$$

A sample profile of the effective angle of attack is shown in Figure 3.1, of which the nominal angle of attack is 20 degrees, the roll frequency is 2 Hz, and the roll amplitude is 30 degrees.

3.1.4 Convective Time and Nondimensional Time. The convective time is the time in which a particle of the flow travels over the reference length scale. Given the free stream speed and the longitudinal characteristic length, the convective time scale in this thesis is calculated as:

$$t_c = \frac{\bar{\bar{c}}}{\bar{U}_\infty} \tag{3.12}$$

Subsequently, the nondimensional time is the dimensionless time, which is normalized by the convective time:

$$t^+ = \frac{t}{t_c} \tag{3.13}$$

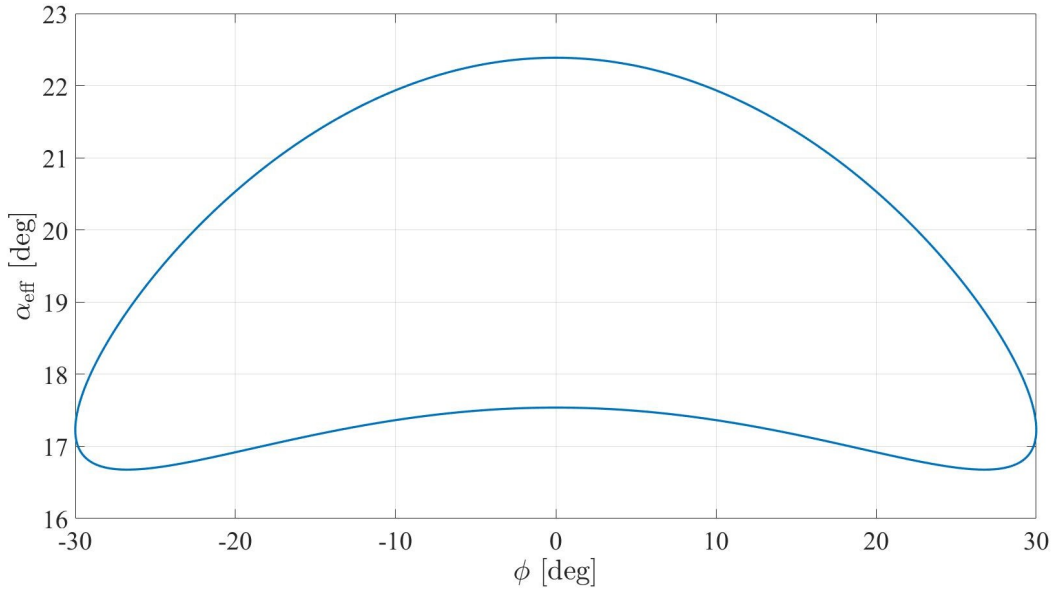

(a) Effective angle of attack vs. roll angle

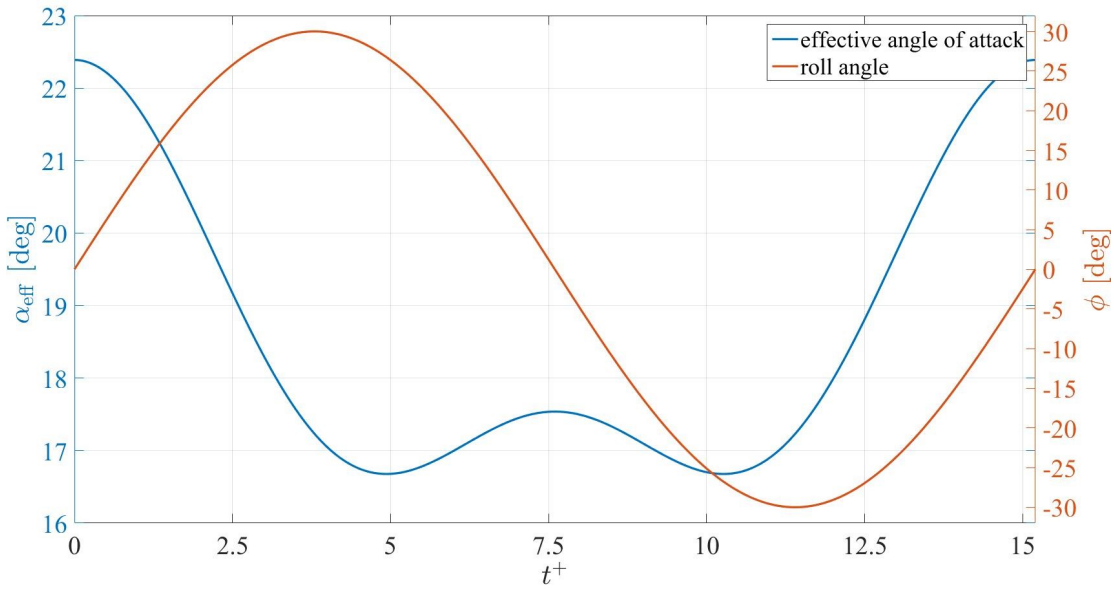

(b) Effective angle of attack (starboard mac) vs. time

Figure 3.1. Example profile of the effective angle of attack

3.2 Steady Baselines

3.2.1 Lift and Drag Coefficients. The lift and drag are measured for the angles of attack from $\alpha = -8°$ to $20°$ with an increment of $2°$, and a roll angle of $\phi = 0$. Normalized by $q_\infty S$, the lift and drag coefficients are shown in Figure 3.2 and Figure 3.3. Both the lift and drag coefficients show typical trends of those on a delta wing within that range of angles of attack [20]. The zero-lift angle of attack is found at $-2°$ with a corresponding drag coefficient of 0.025.

Although the slope of the lift and drag coefficient is slightly greater than those from experiments that were conducted by the Air Force Academy (Appendix B), the difference between the Reynolds numbers is considered to be the cause of this phenomenon. Specifically, the Reynolds number from the Air Force Academy is about 10 times the Reynolds number of this thesis.

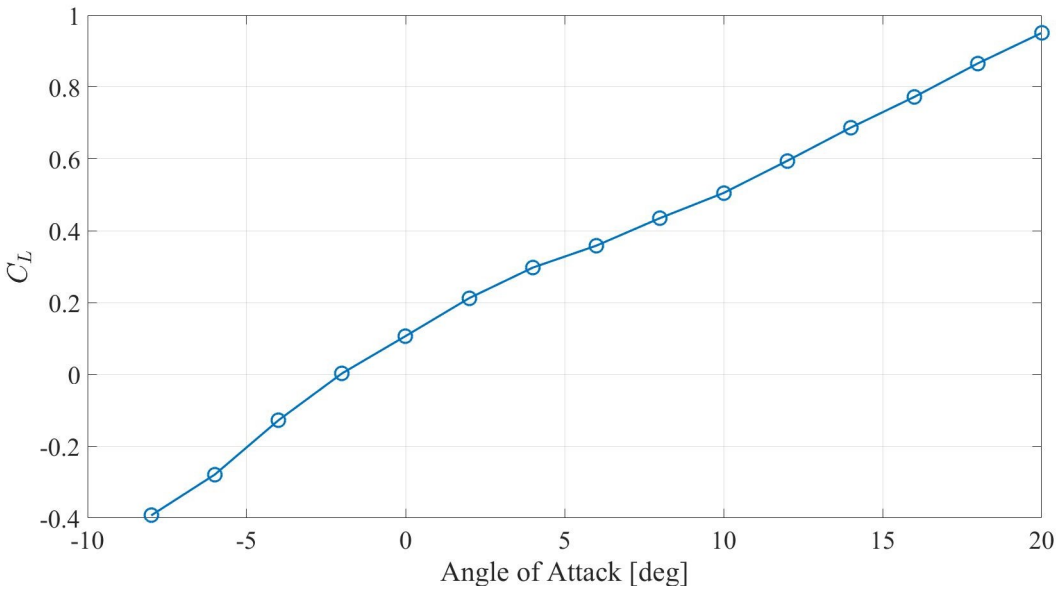

Figure 3.2. Lift coefficient baseline measurement

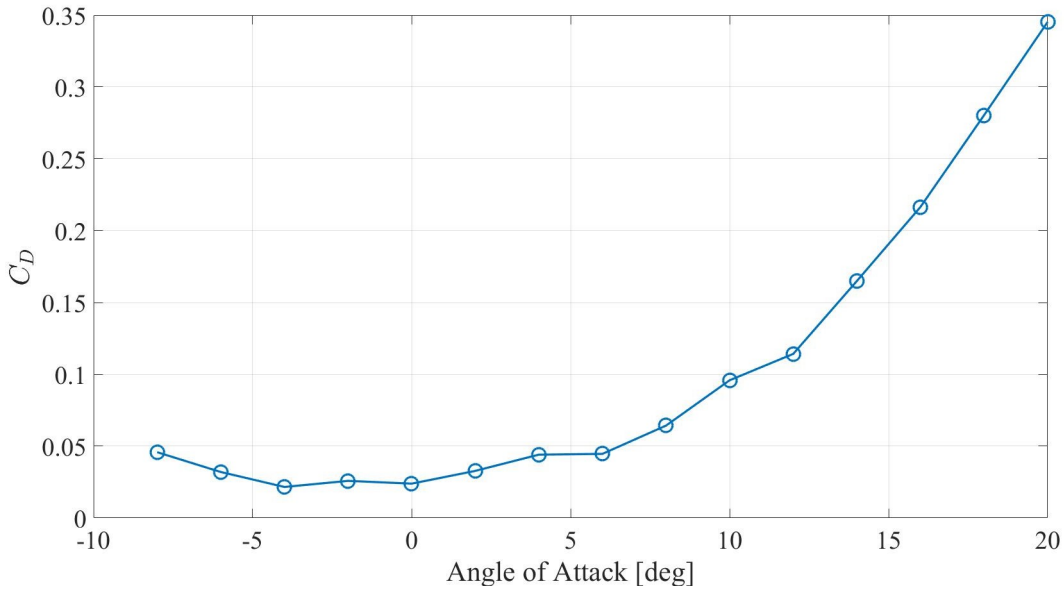

Figure 3.3. Drag coefficient baseline measurement

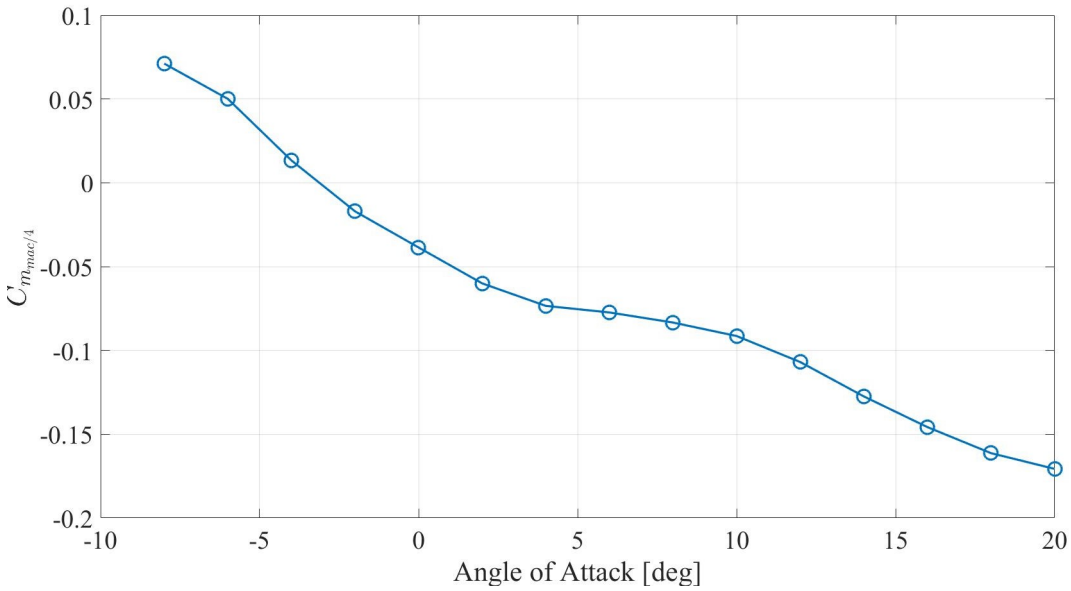

Figure 3.4. Pitch moment coefficient baseline measurement

3.2.2 Pitch Moment Coefficient. As specified in section 1.3.2, the pitch moment is referenced to the quarter mean aerodynamic chord. Figure 3.4 shows that the pitch moment decreases to negative as the angle of attack increases. In most range of angles of attack, the wing undergoes a nose-down moment, which can be explained by the relatively forward-located mac/4 as well as the larger wing area of the after-body. This implies that the aerodynamic center is located further back on the wing.

3.2.3 Pressure Coefficients. The pressure coefficients are the measurements at the 12 pressure sensor locations. As shown in Figure 3.5, most measurement points are dominated by negative pressure coefficients within the range of angles of attack. Especially, at high angles of attack, the slope of pressure coefficients with even numbers increase significantly and give some much more negative values. Considering that the even number pressure sensors are those on the outer edges of the wing (see Figure 2.11), the drop of pressure coefficients implies the presence of leading edge vortex generation on the delta wing [13]. This also provides the possibility for flow field manipulation through active flow control on the edges for roll, pitch, and yaw moments.

The different behavior of the pressure coefficients on the outer edge and of those on the inner top surface are also significant under the dynamic roll conditions, which is discussed in Section 3.3.4.

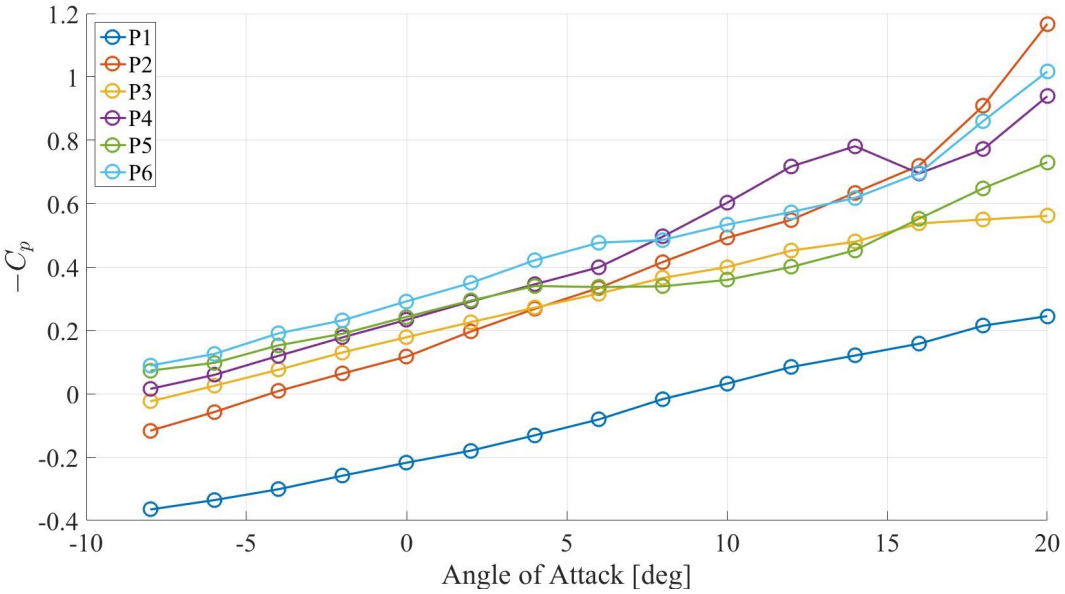

(a) Pressure coefficient baselines on the port

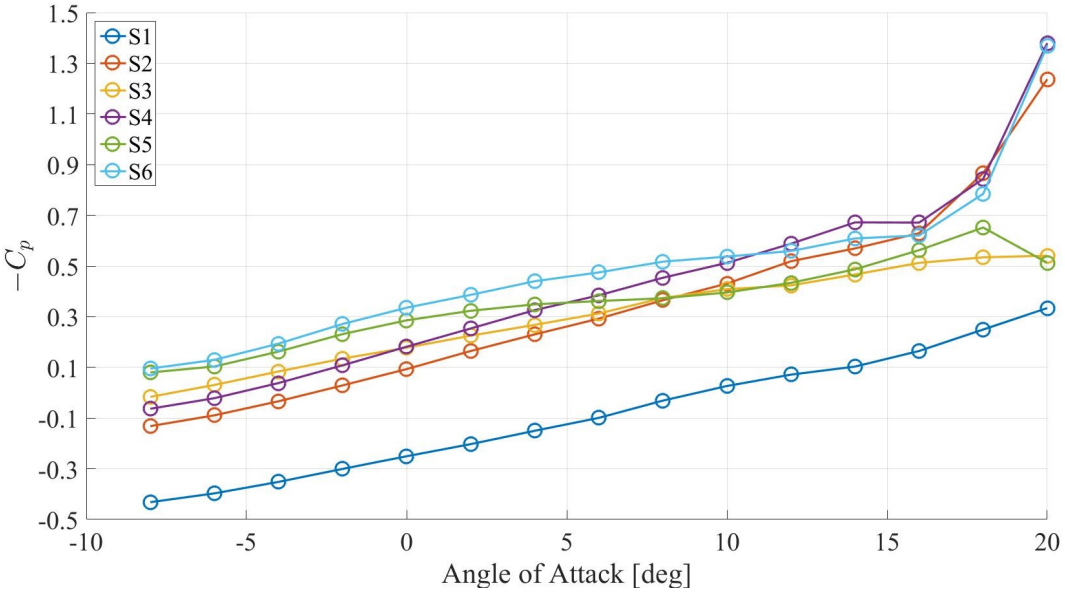

(b) Pressure coefficient baselines on the starboard

Figure 3.5. Pressure coefficient baselines

3.3 Dynamic Roll Measurements

The dynamic roll experiments are conducted at angles of attack of $\alpha = 0$, 5, 10, and 20 degrees. The roll motion uses a sinusoidal function of time:

$$\phi(t) = A\sin(2\pi f t) \tag{3.14}$$

At each angle of attack, measurements are taken for the roll frequencies of $f = 0.5$ Hz, 1.0 Hz, 1.5 Hz, and 2.0 Hz, corresponding to the reduced frequencies, $k = 0.0516$, 0.1033, 0.1550, and 0.2066, which are calculated in Section 3.1.2. In addition, three values of amplitude, $A = 10°,\ 20°$, and $30°$, are tested for different roll frequencies.

3.3.1 Roll Moment Coefficients. The aerodynamic roll moment coefficients of each roll frequency are shown through Figure 3.6 to Figure 3.9. The roll amplitude is 30 degrees. In each figure, two complete cycles of roll moment coefficients of different angles of attack at the same roll frequency are plotted on the same characterized time scale. The solid curves are the roll moment coefficients and the gray dash curve represents the scaled roll angle for the purpose of indicating the real time motion of the wing. A first observation in the results is an increasing trend of the aerodynamic roll moment amplitude corresponding to the rise of the angle of attack. However, the amplitudes only grows slightly from $\alpha = 0°$ to $5°$ and $10°$. For most of the roll frequencies, the roll moment coefficient amplitudes increase less than 0.004 from $\alpha = 0°$ to $10°$. In contrast, there is a big jump on the amplitude when the angle of attack changes from $10°$ to $20°$. Particularly, the roll moment coefficient amplitudes at $\alpha = 20°$ are more than 0.02 greater than those of the lower angles of attack.

On the other hand, the magnitudes of the roll moment coefficients also increase if comparing roll moment coefficients of the higher roll frequencies with those of the lower frequencies. But the amplitudes do not show a obvious jump between different frequencies. These characteristics are summarized in Figure 3.10.

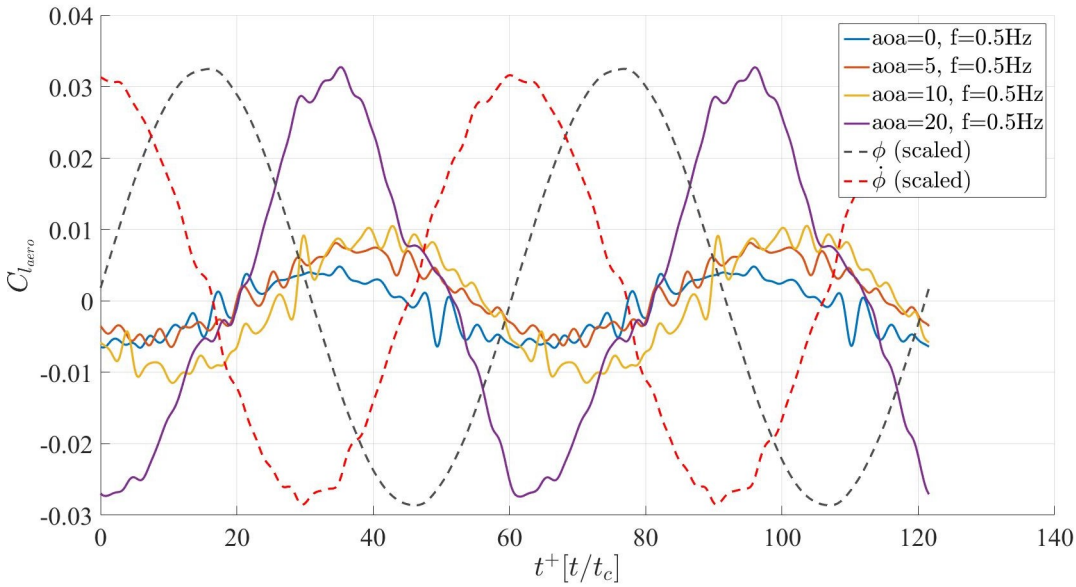

Figure 3.6. Roll moment coefficient of 0.5 Hz cases ($A = 30°$)

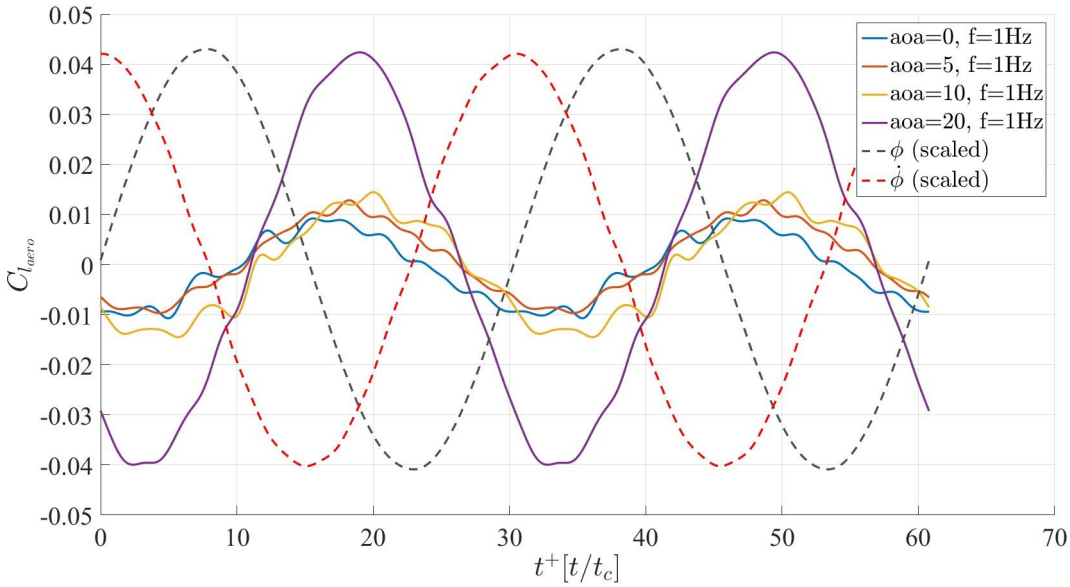

Figure 3.7. Roll moment coefficient of 1.0 Hz cases ($A = 30°$)

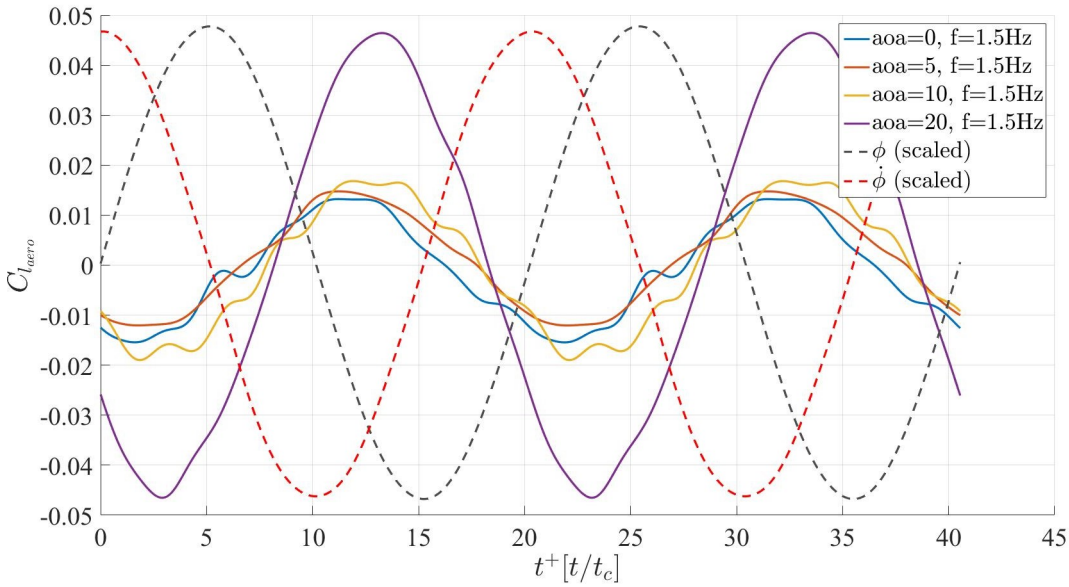

Figure 3.8. Roll moment coefficient of 1.5 Hz cases ($A = 30°$)

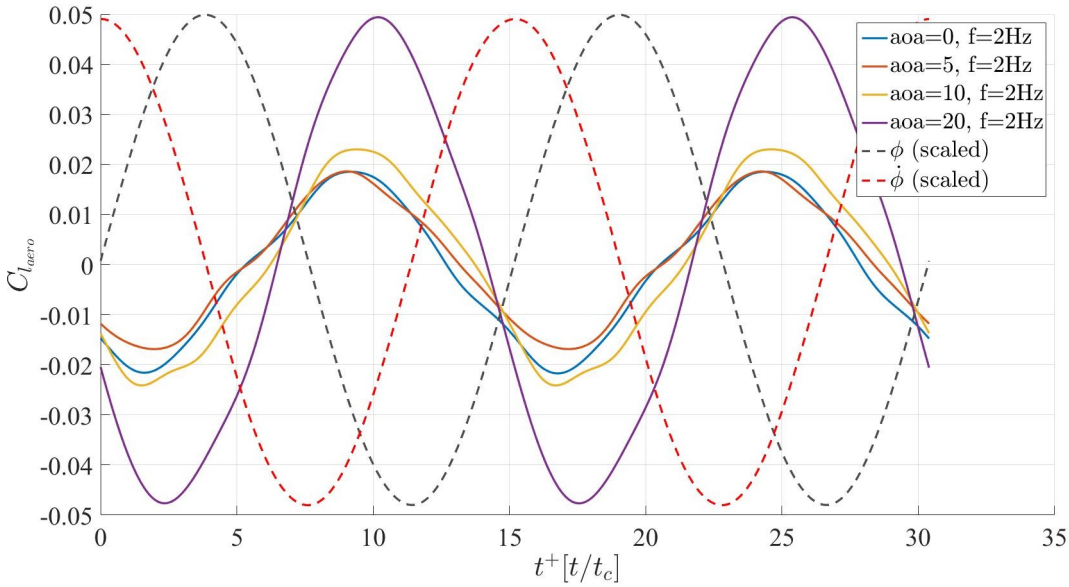

Figure 3.9. Roll moment coefficient of 2.0 Hz cases ($A = 30°$)

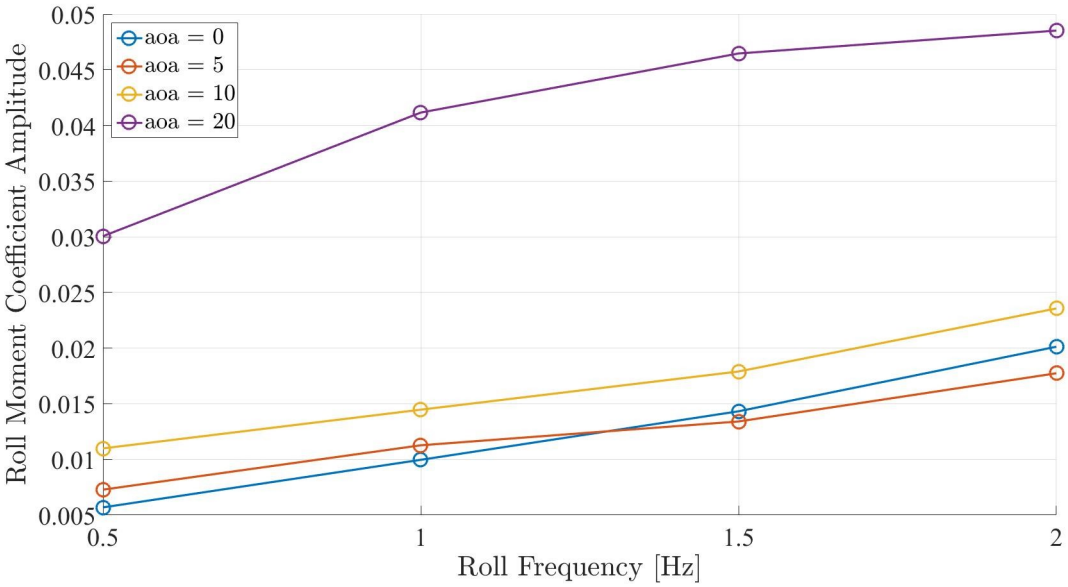

Figure 3.10. Roll moment coefficient amplitude vs. roll frequency ($A = 30°$)

Another characteristic appearing in the roll moment measurements is that there is a phase delay between the roll moment and the roll angle. If we take the first time derivative of the roll angle to obtain the angular velocity, which is the red dash curve in figure 3.6 to Figure 3.9, the phase delay turns out to be connected to the instantaneous roll rates. By taking the Fourier transform, the signals of dominant frequencies are extracted from the measurement data. Then, for each roll frequency, the phase difference between the aerodynamic roll moment and the roll rate can be calculated. Figure 3.11 summarizes the phase angles between the roll moment coefficients and the roll rates. The phase delays of angles of attack at 0° and 20° have growing trends as the roll frequencies increase. For the angles of attack at 5° and 10°, the phase delays first drop at lower roll rates and then start to rise with very small slopes when the roll frequencies reach 2.0 Hz. On the other hand, if comparing the phase delays at a fixed roll rate, the higher angles of attack generally give larger phase delays to the roll moments. This is especially apparent at $f = 1.5$ Hz and 2.0 Hz.

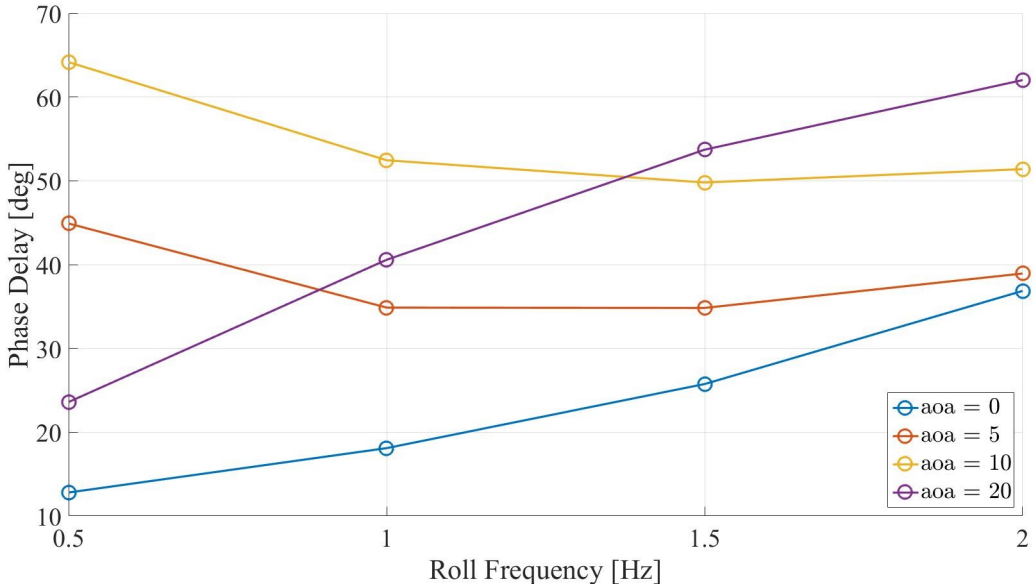

Figure 3.11. Phase delay between the roll moment coefficients and the roll rates ($A = 30°$)

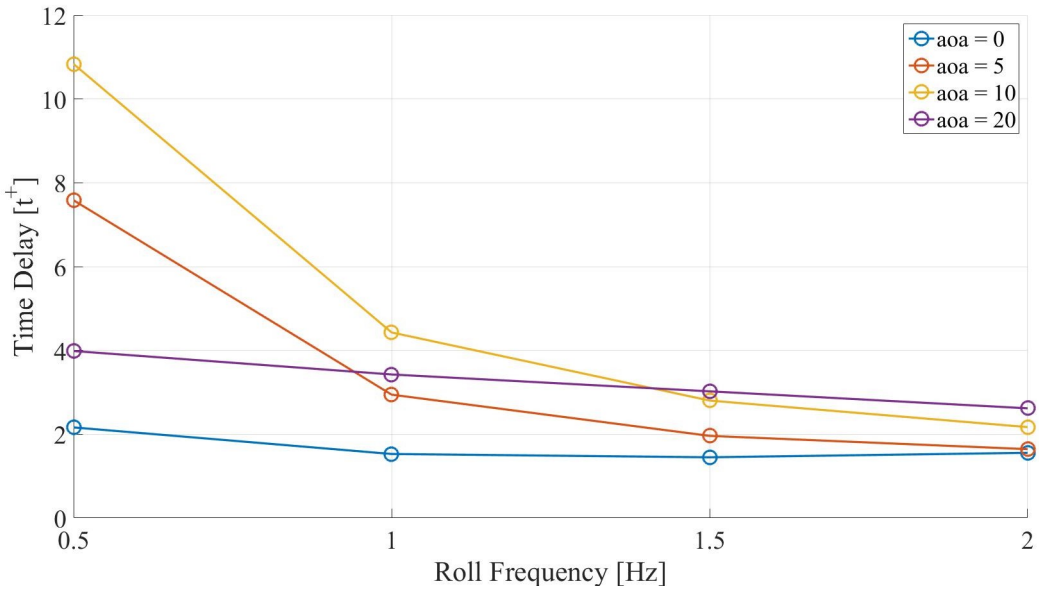

Figure 3.12. Time delay between the roll moment coefficients and the roll rates ($A = 30°$)

For reference, a time delay plot is shown in Figure 3.12. The time delay is obtained from the phase delay calculation, which converts the phase angle into the time difference between the C_l signal and the $\dot{\phi}$ signal for each roll frequency. Then the time delays are nondimensionlized by the convective time t_c. Among all of the angles of attack, the time delays decrease as the roll frequencies increase.

For a fixed angle of attack and a fixed roll frequency, the roll amplitude has an obvious influence on the aerodynamic roll moment coefficients. Example results of two sets of angles of attack and roll frequencies are shown in Figure 3.13 and Figure 3.14. Equation 3.14 and its time derivative give that the angular velocity is proportional to the roll amplitude. The response of the roll moment coefficient to the change of roll amplitude has the same increasing trend. This also verifies that the angular velocity is one of the dominating factors that affects the dynamic roll moment. In addition, the magnitudes of the roll moment response of different roll rates as well as the roll amplitudes give a guideline to the control authority that is needed for the flow actuation, which is discussed in Section 4.3.

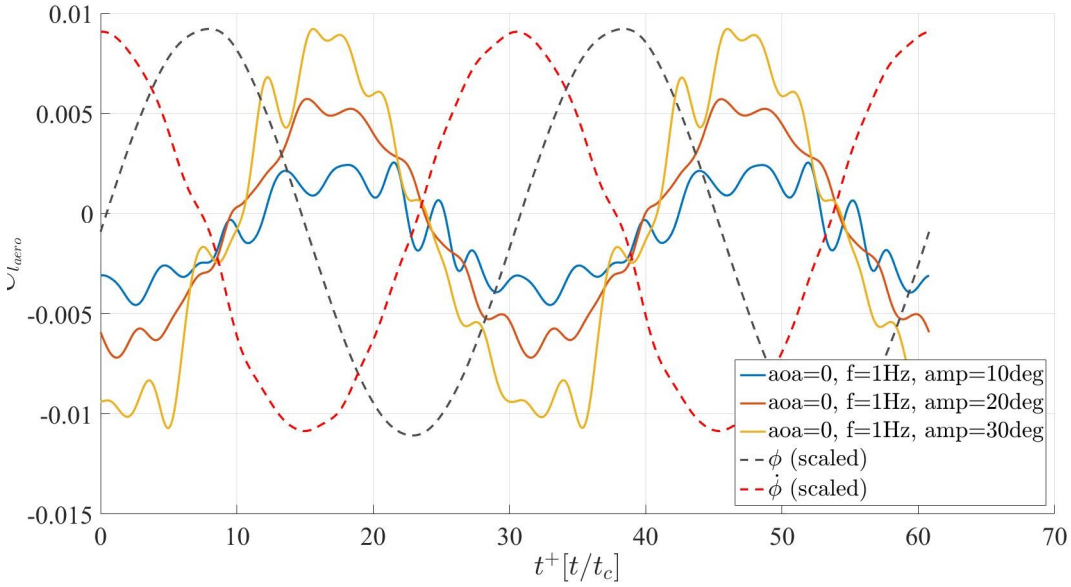

Figure 3.13. Roll moment coefficient of different roll amplitudes at 1.0 Hz (AOA = 0°)

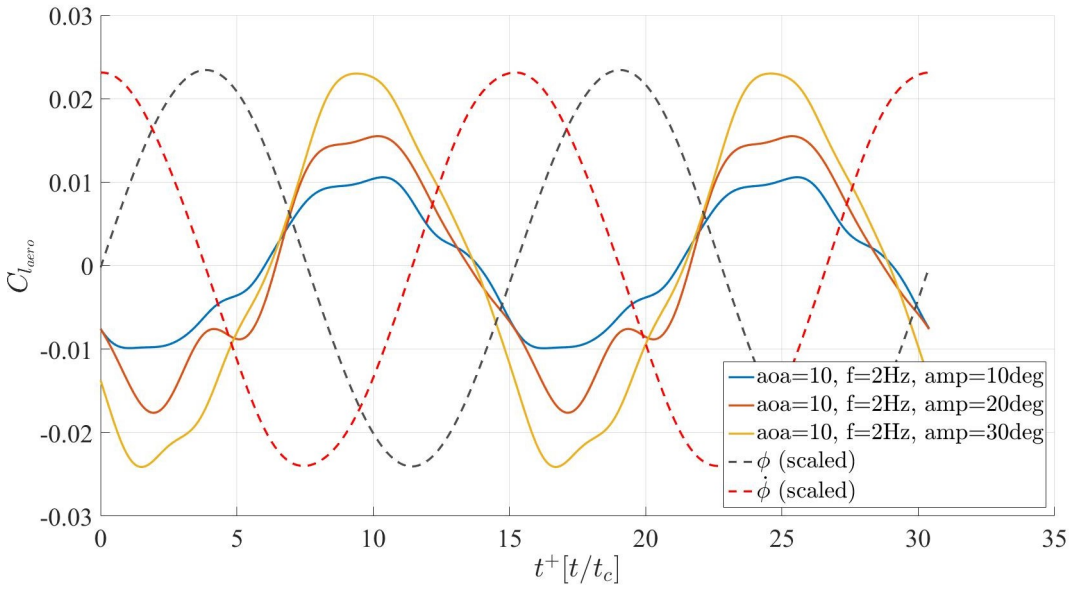

Figure 3.14. Roll moment coefficient of different roll amplitudes at 2.0 Hz (AOA = 10°)

3.3.2 Roll and Pitch Coupling. Some apparent roll-pitch coupling patterns are found at different angles of attack. Figure 3.15 shows the pitch moment coefficient with a roll frequency of $f = 1.0$ Hz at $\alpha = 0°$ angle of attack. The horizontal yellow line is the pitch moment baseline, which is from the measurements in Section 3.2.2. The measurement of the dynamic pitch moment coefficient shows that the roll motion generates a greater nose-down moment when the wing is rolling at 0° angle of attack. However, the measurement from a little higher angle of attack shows an opposite trend of change on the pitch moment. Figure 3.16 shows the pitch moment coefficient that is measured under the same condition as that in Figure 3.15 with a different angle of attack at 5°. In the 5° case, the roll motion provides the wing with a nose-up moment.

The shift on the pitch moment coefficient is not obvious when the angle of attack gets to higher degrees. A comparison among the angles of attack at 5°, 10°, and 20° is shown through Figure 3.17 to Figure 3.19, in which the roll frequencies are 2.0 Hz for all of them. Although the roll frequency is doubled in the 5° angle of attack case, the reduction of the mean pitch moment coefficient is as significant as that of the 1.0 Hz case. In contrast, the pitch moment coefficients do not shift in the 10° and 20° cases.

One of the causes of the complex behavior of the pitch moment is considered to be related to the change of the effective angle of attack. The effective angle of attack at 5° nominal angle of attack varies from 2.42° to 7.56°, while the ranges of the effective angles of attack at 10° and 20° nominal angles of attack are 7.43° to 12.52° and 16.68° to 22.39°. This difference of effective angles of attack along with the shift of the pitch moments imply that the flow field over the wing is more sensitive to the change of the angle of attack when the the wing has smaller incidence. A hypothesis that needs to be verified is that the vortex generation is less stable at lower angles of

attack, while the leading edge vortex is dominating the aerodynamic forces at higher angles of attack.

Given the difference between these cases, a common characteristic of the pitch moment coefficients from most of the experiments is that the wing tends to experience a greater nose-down moment when it rolls to the zero-degree roll angle at which the the wing has the maximum instant roll rate. The discussion about the lift coefficient in Section 3.3.3 gives a possible explanation for this behavior.

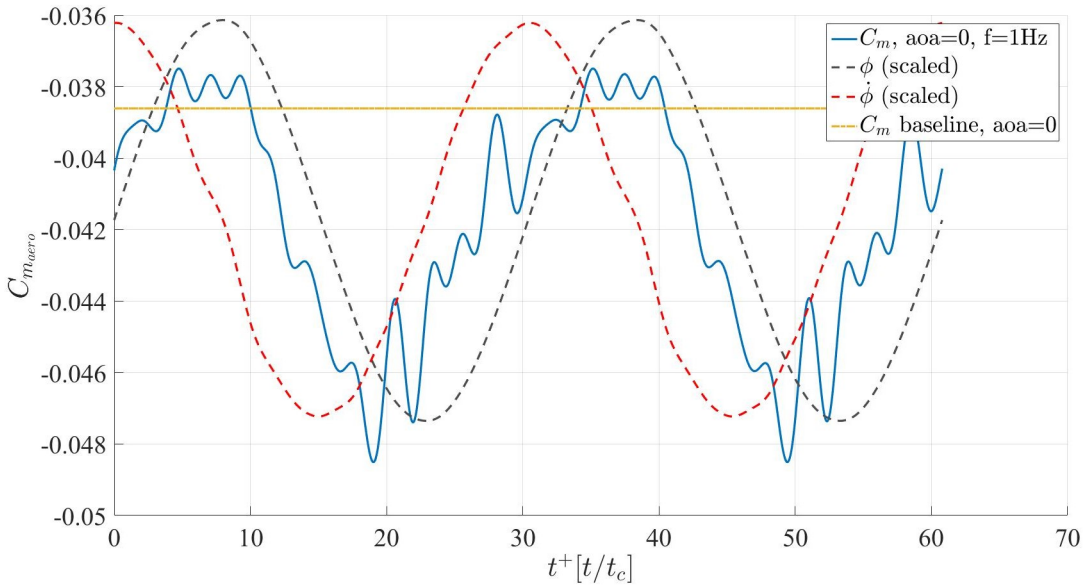

Figure 3.15. Pitch moment coefficient at 1.0 Hz (AOA = 0°)

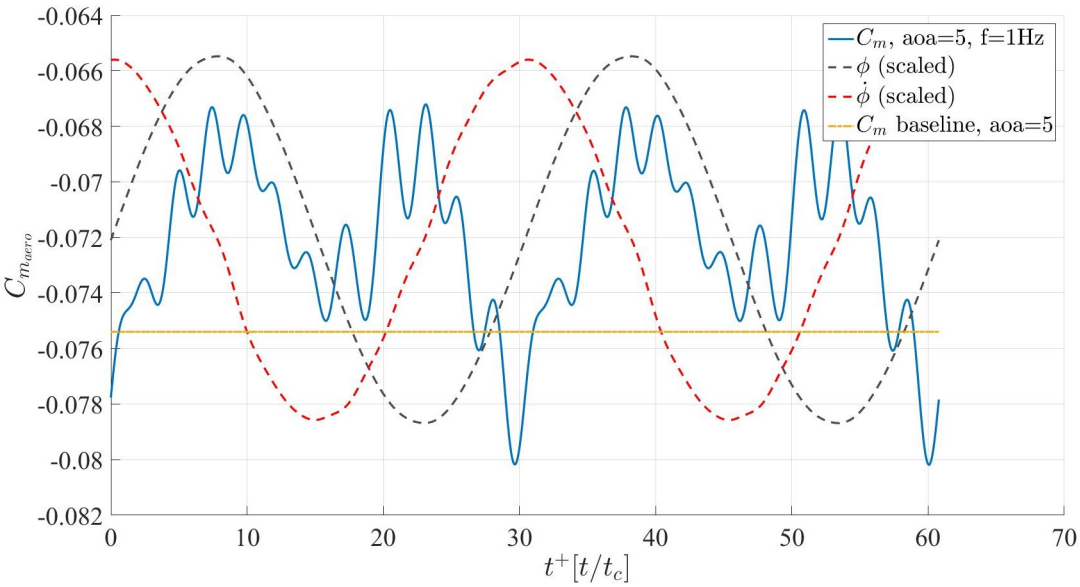

Figure 3.16. Pitch moment coefficient at 1.0 Hz (AOA = 5°)

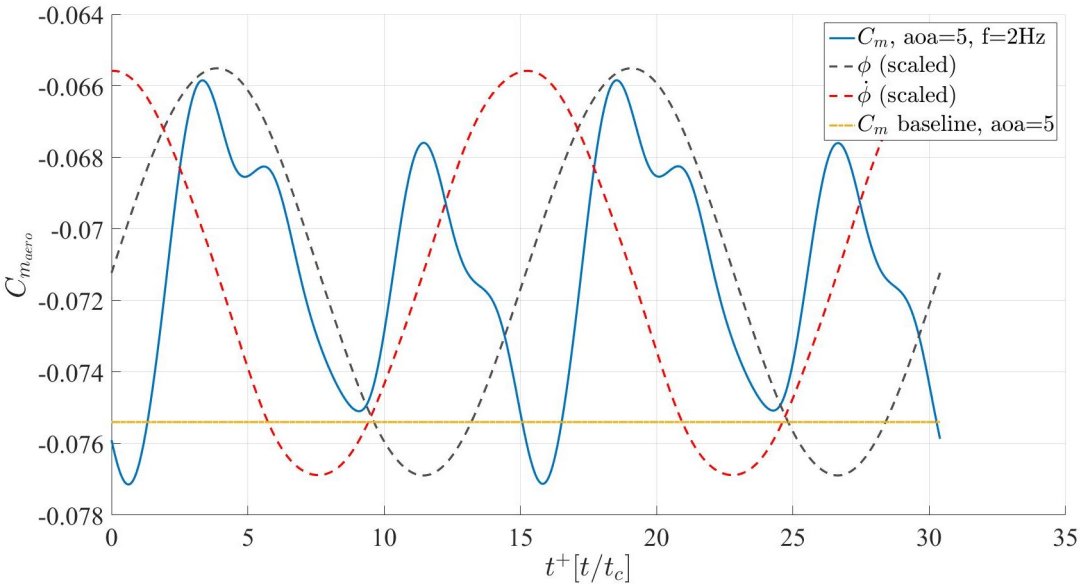

Figure 3.17. Pitch moment coefficient at 2.0 Hz (AOA = 5°)

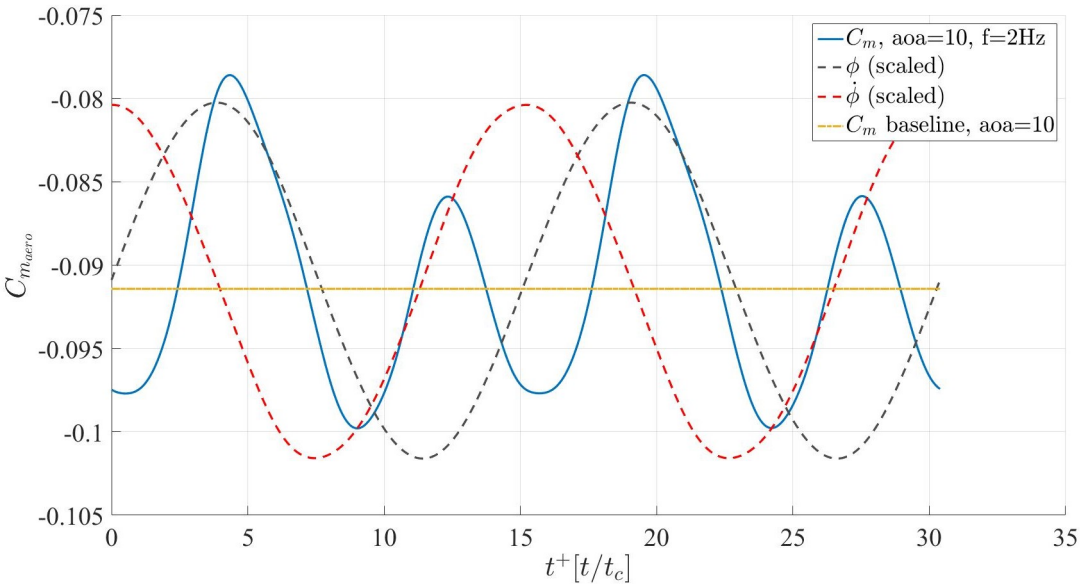

Figure 3.18. Pitch moment coefficient at 2.0 Hz (AOA = 10°)

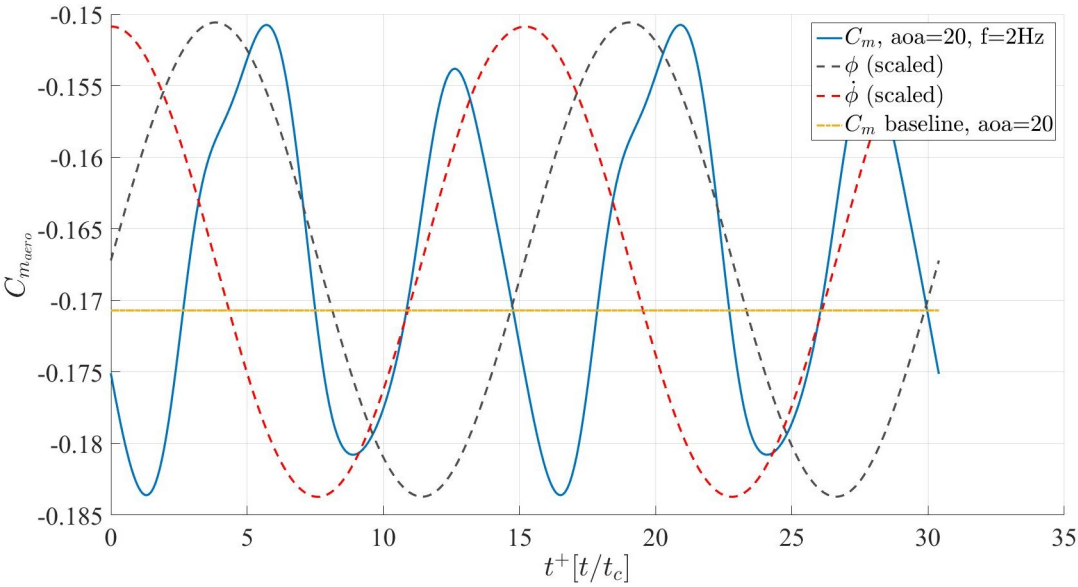

Figure 3.19. Pitch moment coefficient at 2.0 Hz (AOA = 5°)

3.3.3 Dynamic Lift Coefficient. Similar to the pitch moment coefficient, the lift coefficient is strongly affected by the angle of attack. Figure 3.20 shows the dynamic lift coefficient of zero-degree angle of attack at a roll rate of 2.0 Hz. The steady state lift coefficient baseline is plotted as the horizontal yellow line, the roll angle and the roll rate are the dash curves behind the blue lift coefficient curve. The lift coefficient at zero-degree angle of attack shows four oscillations per cycle of roll, while the lift coefficients at higher angles of attack, as shown in Figure 3.21 and Figure 3.22, have apparent patterns within a roll cycle.

The shifts of the mean values of the lift coefficients to smaller values at higher angles of attack implies that the total lift may be lost when the wing is rolling at these angles of attack. Nevertheless, the lift coefficient reaches its maximum value when the wing passes the zero-degree roll angle with a maximum value of roll rate. This helps explain the greater nose-down moment which was mentioned in Section 3.3.2, since the quarter mean aerodynamic chord moment reference point is upstream direction of the aerodynamic center thus the lift generates the negative pitch moment.

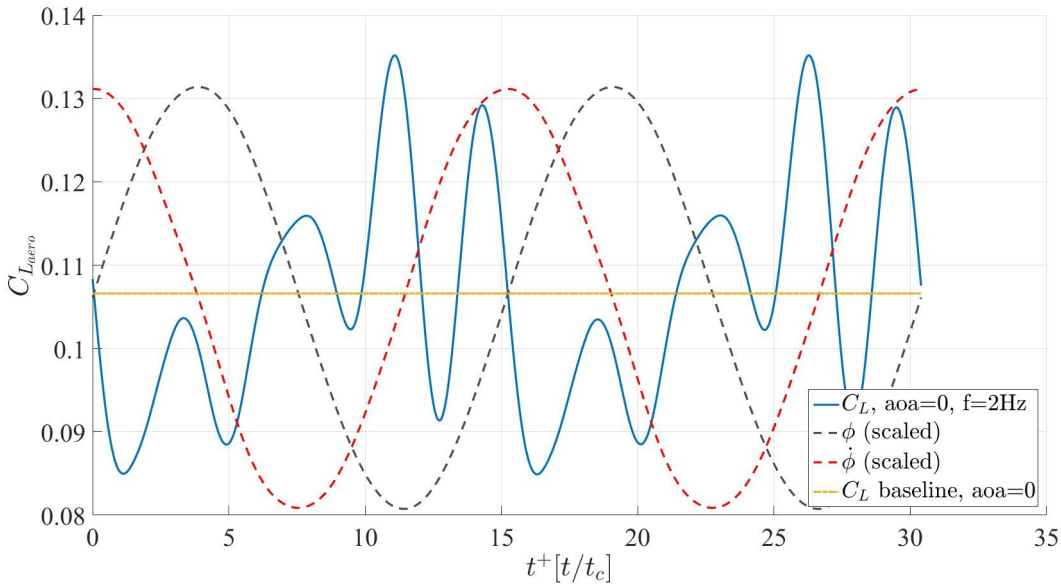

Figure 3.20. Lift coefficient at 2.0 Hz (AOA = 0°)

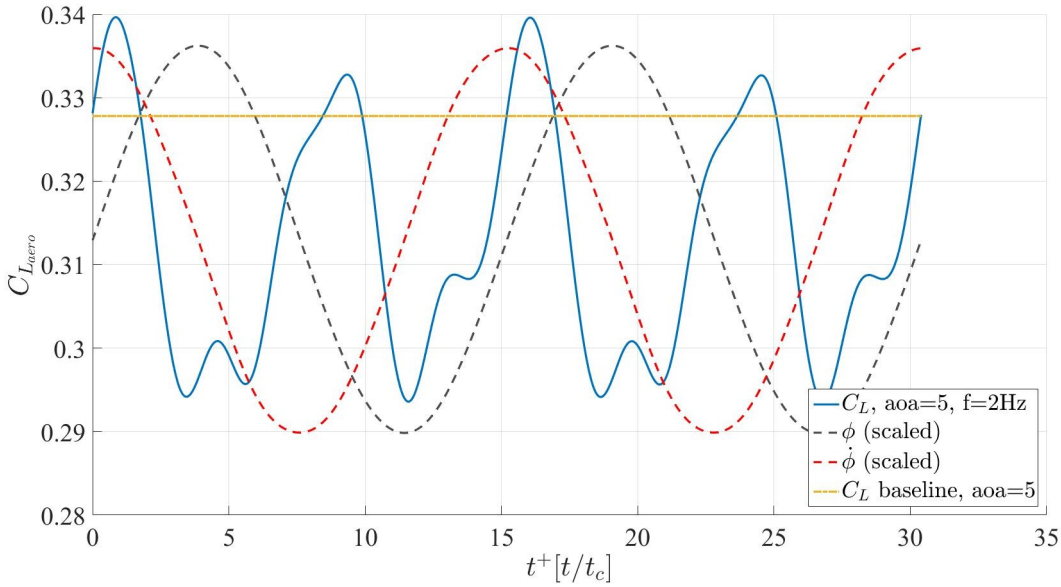

Figure 3.21. Lift coefficient at 2.0 Hz (AOA = 5°)

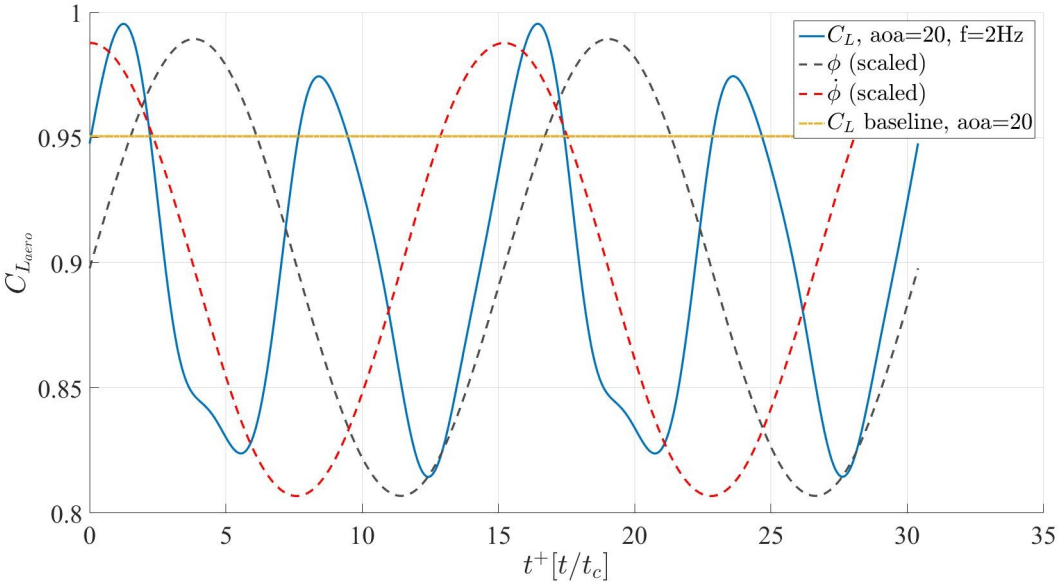

Figure 3.22. Lift coefficient at 2.0 Hz (AOA = 20°)

3.3.4 Dynamic Pressure Coefficients. The force and moment coefficients are integral quantities. The pressure data can provide insight into details of the flow. Under the dynamic roll conditions, the pressure coefficients have different behaviors on the outer and the inner wing surface. For most of the angles of attack, especially at lower angles of attack, the pressure coefficients change anti-symmetrically on the outer wing, which is closer to the leading edge vortex. In the meantime, the pressure coefficients of the inner surface of the wing are not affected by the asymmetry of the roll motion, as they vary in a synchronized pattern. Examples of the pressure coefficient measurements are shown in Figure 3.23. In the plots, the pressure coefficients that are labeled with "P" are the measurements from the port (left) side of the wing. Similarly, those are labeled with "S" are from the starboard (right) side. In addition, all these pressure coefficients are measured at the same longitudinal position and those with a number 6 are closer to the leading edges while those with a number 5 are on the inner part of the wing.

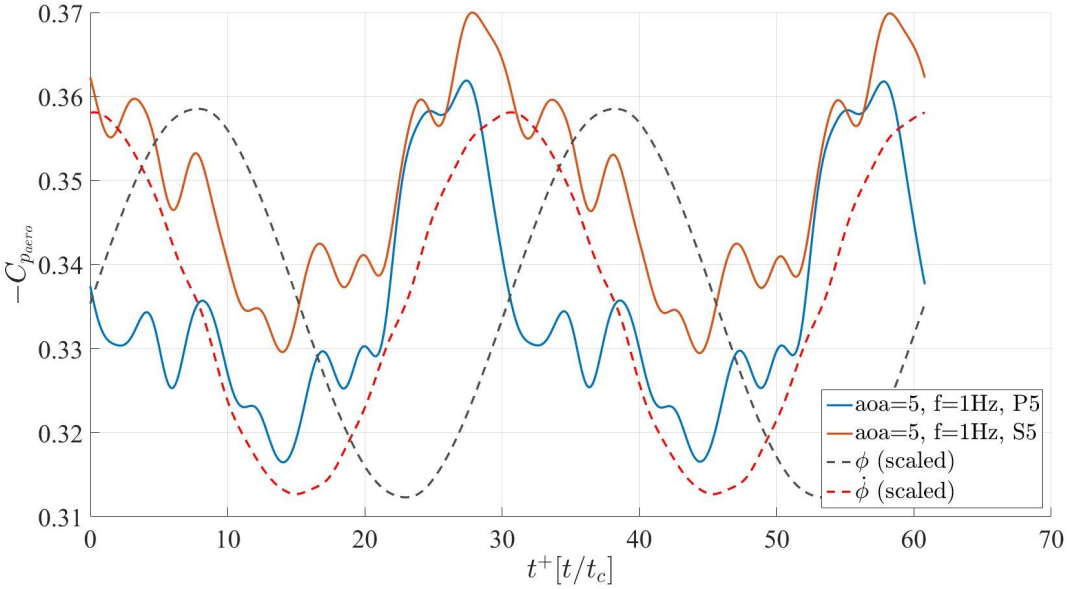

(a) Inboard pressure coefficient measurements

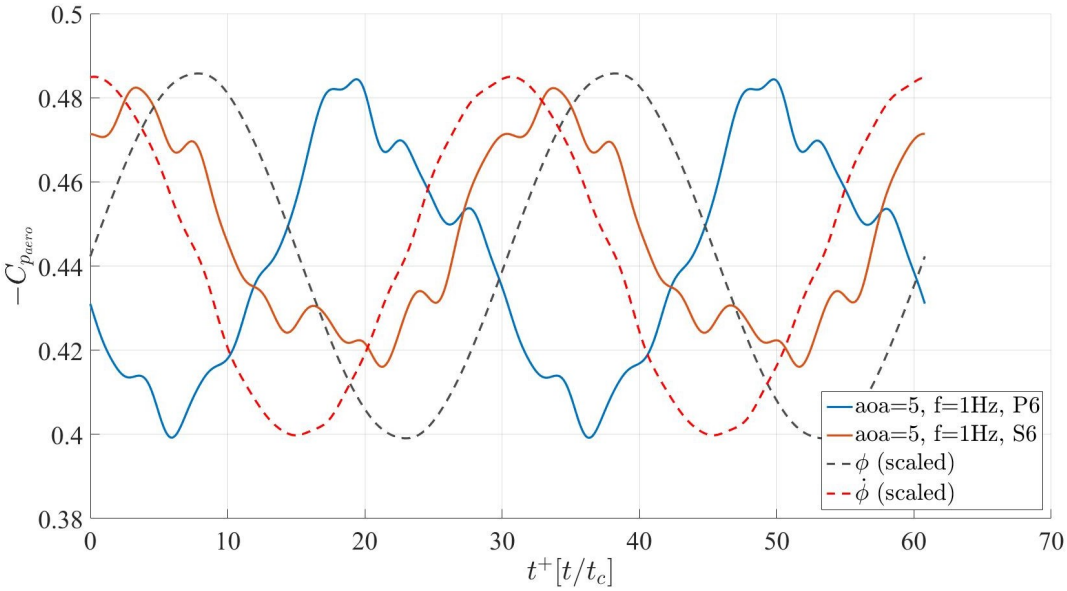

(b) Outboard pressure coefficient measurments

Figure 3.23. Pressure coefficient measurements at 1.0 Hz (AOA = 5°)

3.4 Smoke Wire Flow Visualizaiton

In order to have a visual observation on the flow field, smoke wire visualization is conducted for some selected angles of attack that are of the interest. The smoke is generated by a vertical smoke wire in the upstream and the smoke forms a smoke sheet that is parallel to the side of the test section of the wind tunnel. A camera that is synchronized with the movement of the smoke sheet takes pictures from the side in a way that the focal plane overlaps with the smoke sheet. The smoke sheet passes over the wing at several distances from the root chord, so that the flow visualization helps to provide better understanding of a 3-D flow field over the wing. In the experiments, the distances are chosen as: $y_s = 0.1s$, $y_s = 0.5s$, $y_s = 0.66s$ ($\frac{2}{3}s$), and $y_s = 0.9s$.

Two angles of attack, $\alpha = 5°$ and $10°$, are selected to conduct the flow visualization. The case of $\alpha = 5°$ is a moderate representation of small angle of attack while the $\alpha = 10°$ shows the flow field of a moderately high angle of attack case. Despite the difference between the angles of attack, all of the other conditions including free stream speed, roll rate, the roll angle at which the pictures are taken, are kept the same, in order to make valid comparison between these angles of attack.

3.4.1 Steady Flow Field. Figure 3.24 shows the flow field over the steady wing at $\alpha = 5°$ and $10°$. The flow is found to be fully attached on the wing at $5°$ angle of attack while it is separated and curled inward at $10°$ angle of attack.

Through moving the smoke sheet inward and outward, several photos construct a pseudo 3-D visualization of leading edge vortex shedding on the delta wing, as shown in Figure 3.25 for $\alpha = 10°$. Figure 3.25 (a) shows that the flow remains attached on the inner part of the wing. Nevertheless, Figure 3.25 (b), (c), and (d) demonstrate that the flow is bent toward the wing root and the vortex grows along the swept leading edge forming a strong vortex over the trailing edge.

(a) AOA = 5°, $y_s = 0.66s$

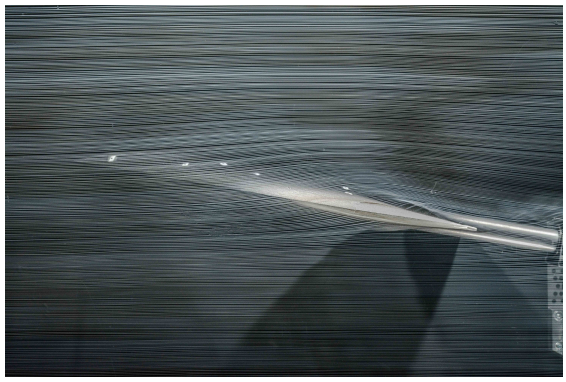

(b) AOA = 10°, $y_s = 0.66s$

Figure 3.24. Smoke wire visualization of the steady wing

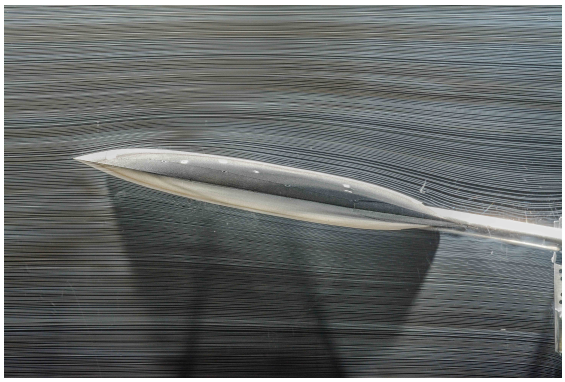

(a) $y_s = 0.1s$

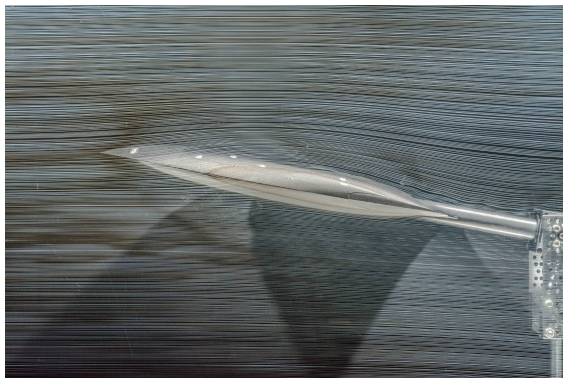

(b) $y_s = 0.5s$

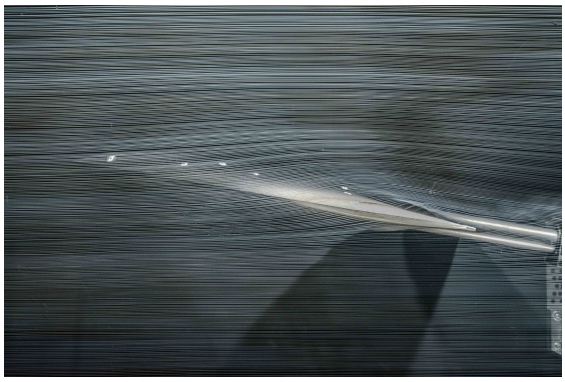

(c) $y_s = 0.66s$

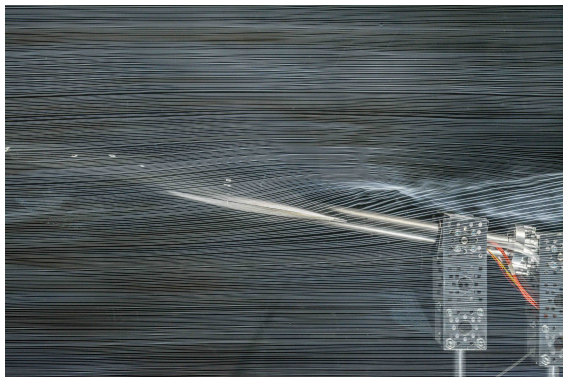

(d) $y_s = 0.9s$

Figure 3.25. Smoke wire visualization of the leading edge vortex at 10° angle of attack

3.4.2 Dynamic Roll. To help understand the lift and pitch moment at zero-degree roll angle, the smoke wire visualization is also processed for a few sets of dynamic roll cases. The camera, the smoke sheet, and the roll motion are synchronized, so that the flow field at the desired roll angle and roll rate can be visualized through this technique.

(a) $y_s = 0.1s$

(b) $y_s = 0.5s$

(c) $y_s = 0.66s$

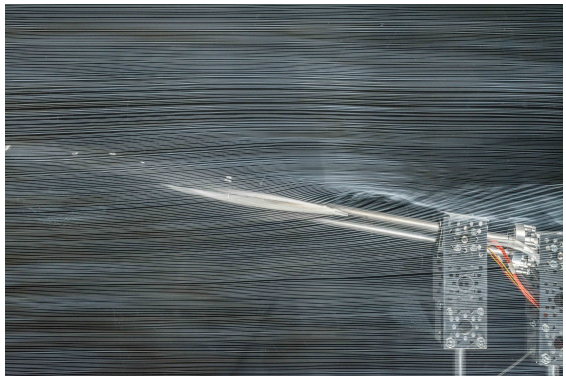

(d) $y_s = 0.9s$

Figure 3.26. Smoke wire visualization of the dynamic rolling at 1.5 Hz with positive angular velocity, 10° angle of attack

Figure 3.26 and Figure 3.27 give a set of sample photos of the dynamic rolling, of which the angle of attack is 10 degrees and the roll frequency is 1.5 Hz. The smoke sheet is placed on the port side of the wing. At each smoke sheet distance, photos are taken when the wing has a positive (left wing rolling up) (Figure 3.26) and negative (Figure 3.27) roll rate. In other words, the photos show the flow field when the wing rolls the fastest to the starboard or to the port.

The flow field visualization partially verifies the hypothesis from Section 3.3.2 about the influence of the effective angle of attack on the vortex generation, subsequently, the change of lift and pitch moment. When the wing rolls positively, the port side of the wing is moving upward which causes the effective angle of attack to reduce. As a result, the flow separation and the vortex shedding are suppressed on the top of the wing. This is more apparent where the smoke sheet is closer to the tip of the wing, since the change of the effective angle of attack is more significant. In addition, the comparison between Figure 3.26 (c), (d) and Figure 3.25 (c), (d) reinforces the conclusion.

On the other hand, the effective angle of attack of the port side wing increases as the it rolls negatively (left wing moving downward). By comparing Figure 3.27 (b) with Figure 3.26 (b), the flow is found to be rolling inward more. Figure 3.27 (c) and (d) demonstrate the consequence of a higher effective angle of attack near the wing tip. The vortex is generated along the leading edge and the flow does not fully separate until it reaches the very tip of the wing.

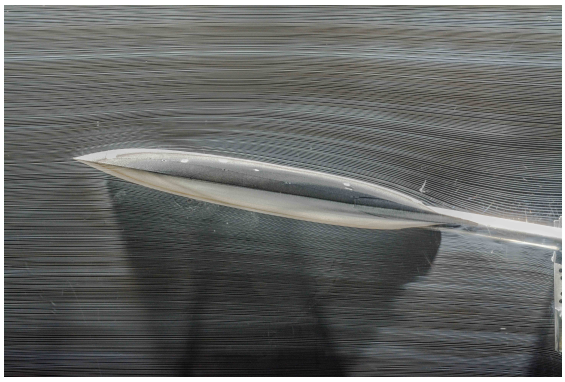

(a) $y_s = 0.1s$

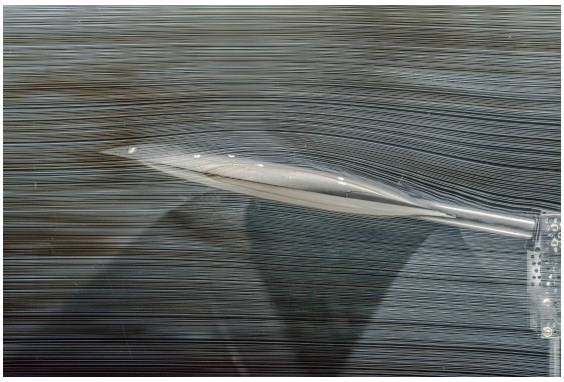

(b) $y_s = 0.5s$

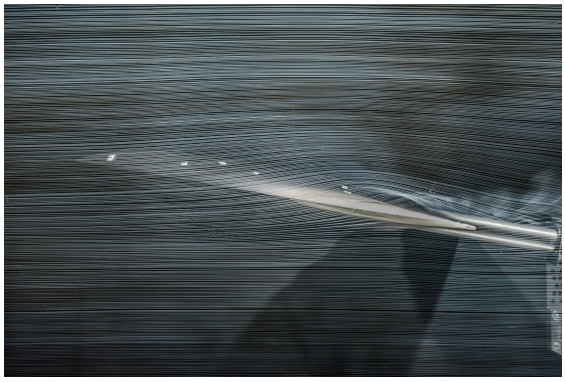

(c) $y_s = 0.66s$

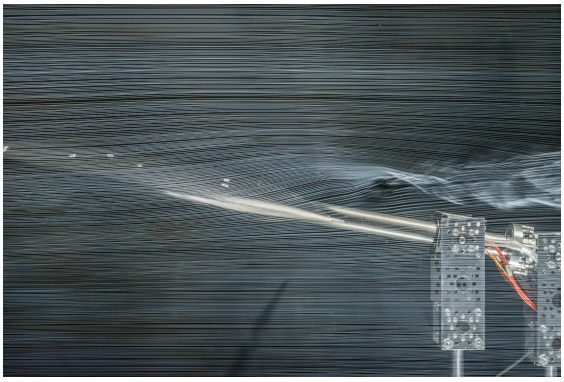

(d) $y_s = 0.9s$

Figure 3.27. Smoke wire visualization of the dynamic rolling at 1.5 Hz with negative angular velocity, 10° angle of attack

CHAPTER 4
ACTUATION TESTS

The active flow control actuators are tested on the wing under a steady condition, in order to examine the control characteristics of the actuators. Utilizing the actuation configuration from Section 2.6.1 and Section 2.6.2, the input of the actuation is the voltage to the proportional valves and the voltage is converted into the momentum coefficient by Equation 2.8 and Equation 2.9. The output of the actuation is considered to be the change of the moment coefficients on the wing.

4.1 Static Maps

The static maps of the actuation are obtained by conducting a quasi-steady actuation on the wing and measuring the inputs and outputs. The input voltage varies as a sinusoidal signal with a 0.01 Hz frequency. The proportional valves are tuned to have the same level of response to the same input voltage. After the tuning, the port actuator and the starboard actuator are tested separately to obtain the static map measurements.

4.1.1 Roll Moment Coefficient Static Map. Figure 4.1 gives the static map for the roll moment coefficient responding to the quasi-steady actuation at 20° angle of attack. The x-axis is the momentum coefficient as the input and the y-axis is the change of the roll moment coefficient due to the actuation. Since the jet flow from the actuators shoots downward, the actuation on the port side generates a positive roll moment and the actuation on the starboard does the opposite. The response of ΔC_l is symmetric on the two sides and has a range of 0 to 0.02. The ΔC_l appears in a loop as the input increases and decreases. This is due to the hysteresis performance of the proportional valve when the orifice opens and closes with a continuous increasing or decreasing current, which leads to a shift on the mass flow rate as [Appendix] shows.

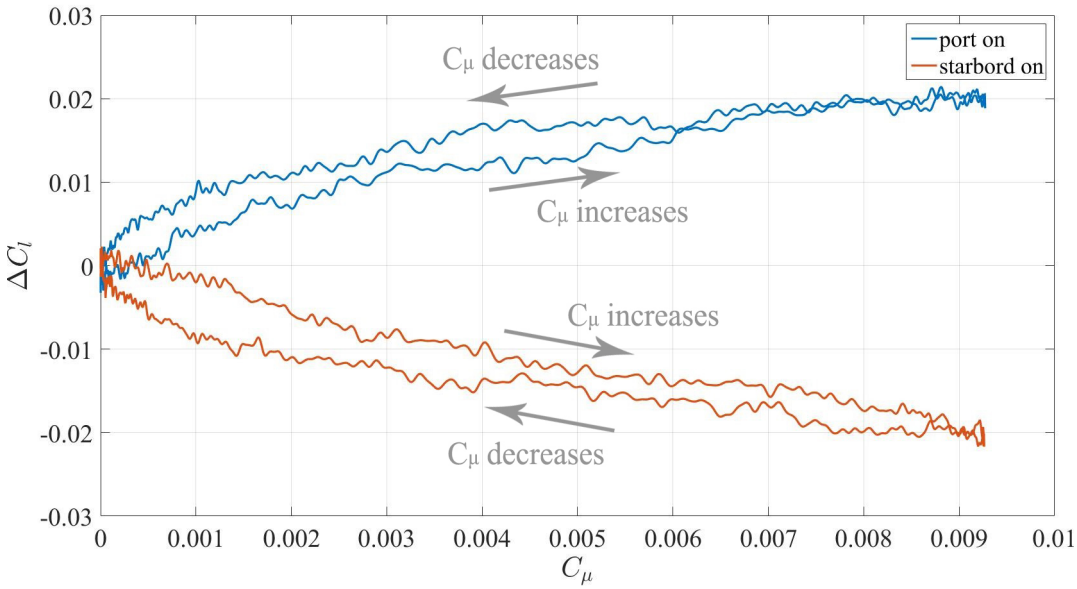

Figure 4.1. Roll moment coefficient static map of the actuation

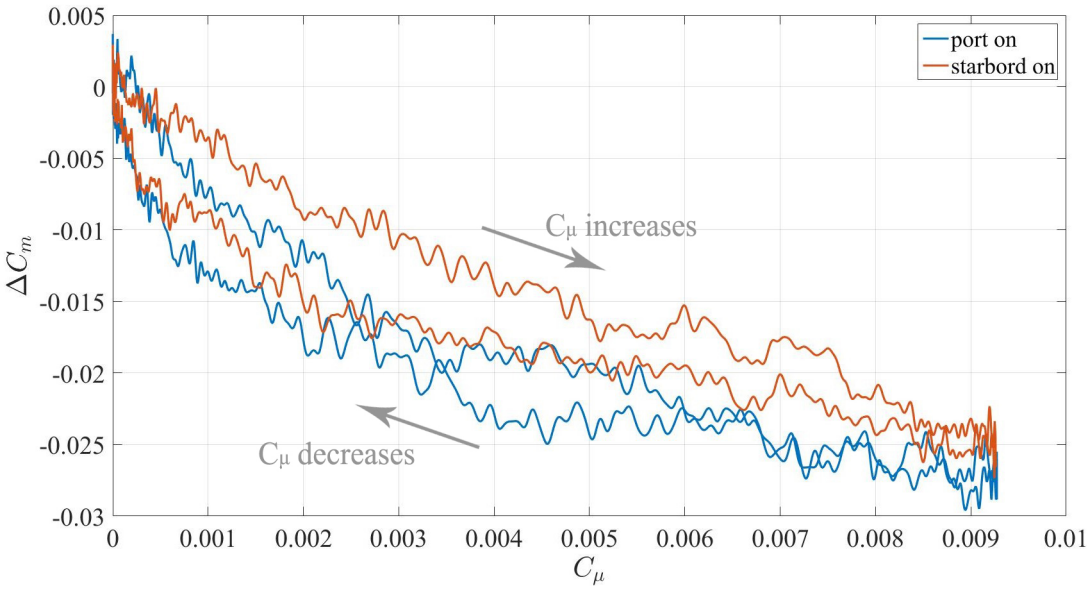

Figure 4.2. Pitch moment coefficient static map of the actuation

4.1.2 Pitch Moment Coefficient Static Map. The pitch moment coefficient static map corresponding to the actuation at 20° angle of attack is shown in Figure 4.2. Since the actuation is on the trailing edge of the wing, it generates a nose-down moment. From the measurements, a single actuator is able to provide a $\Delta C_m = -0.025$ at maximum input level. therefore, the active flow actuation has a range of ΔC_m from 0 to -0.05.

4.2 Dynamic Response

The dynamic response of the actuation is important for the design of the control system. The roll moment responses to the dynamic actuation on the steady wing are measured at different angles of attack and under different actuation frequencies. Figure 4.3 to Figure 4.5 show the roll moment coefficient responses at 0°, 10°, and 20° angle of attack. The results show that the upper limits of ΔC_l under dynamic actuation are lower than those in the static map for every angle of attack. However, the hysteresis loops increase as the actuation frequency increases.

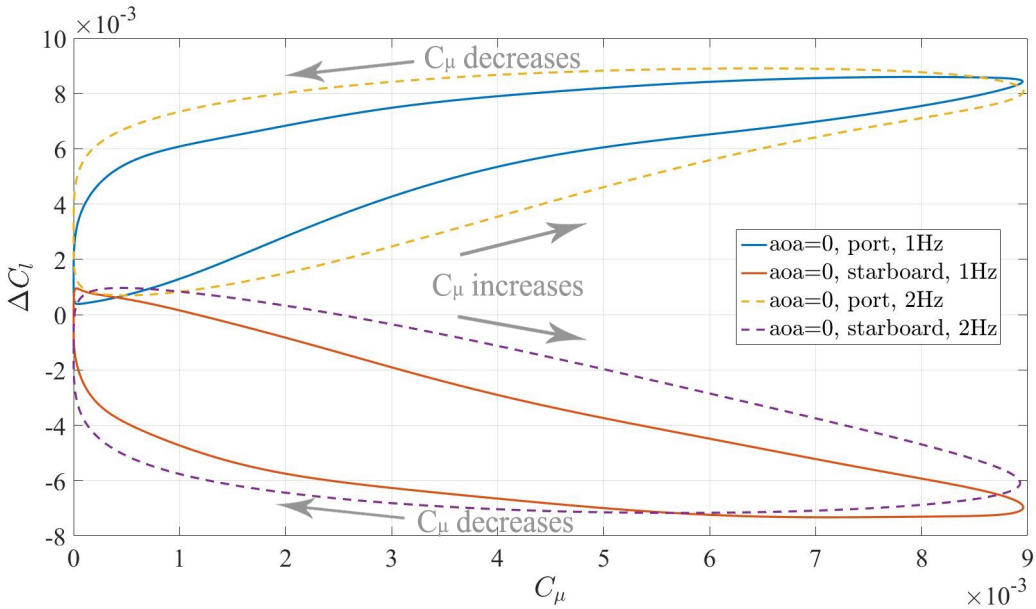

Figure 4.3. Roll moment coefficient response to dynamic actuation at 0° angle of attack

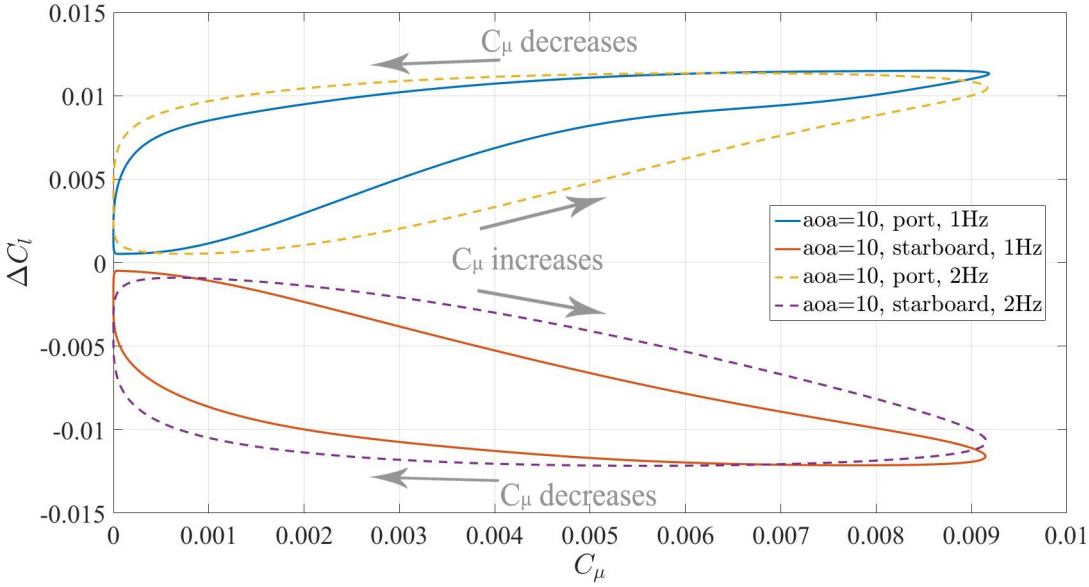

Figure 4.4. Roll moment coefficient response to dynamic actuation at 10° angle of attack

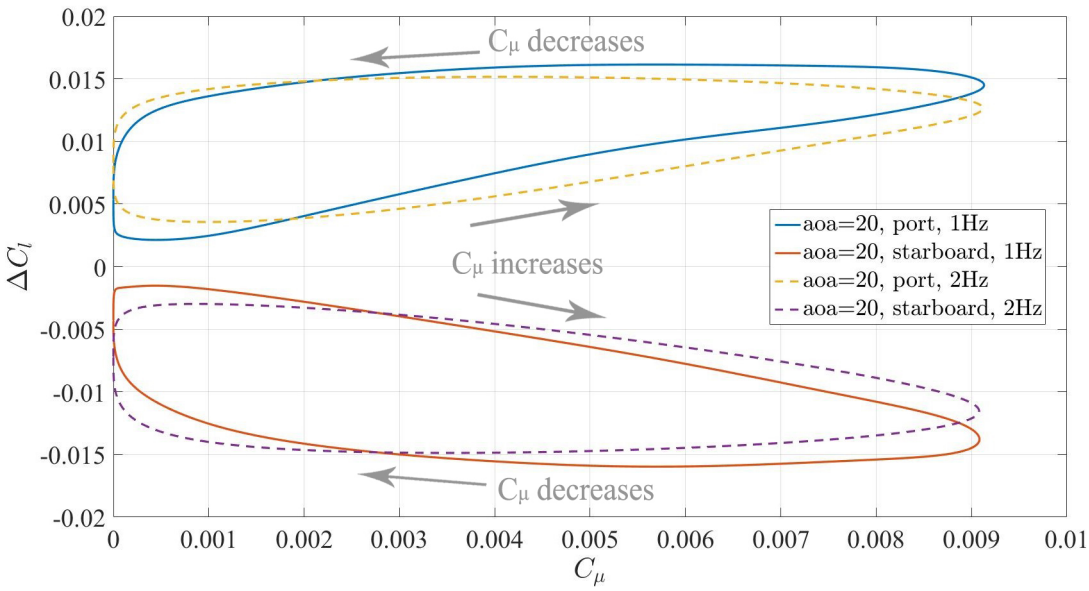

Figure 4.5. Roll moment coefficient response to dynamic actuation at 20° angle of attack

4.3 Control Authority on the Roll Moment

As another guidance to the design of the control system, the control authority of the actuation on the roll moment coefficient needs to be examined. Combining the results of aerodynamic roll moment coefficients of different roll amplitudes from Section 3.3.1 and the results of the roll moment coefficient responses to the dynamic actuation from Section 4.2, the control limits of the actuation at different angles of attack, roll rates, and roll amplitudes can be obtained.

Figure 4.6 and Figure 4.7 are examples of the controllability examinations. The solid lines are the ΔC_l which is generated by the actuation, and the dash lines are the aerodynamic moment under different roll amplitudes at the same angle of attack and roll frequency. The actuation is able to give control to the aerodynamic roll moment coefficient within the envelopes that are bounded by the solid lines.

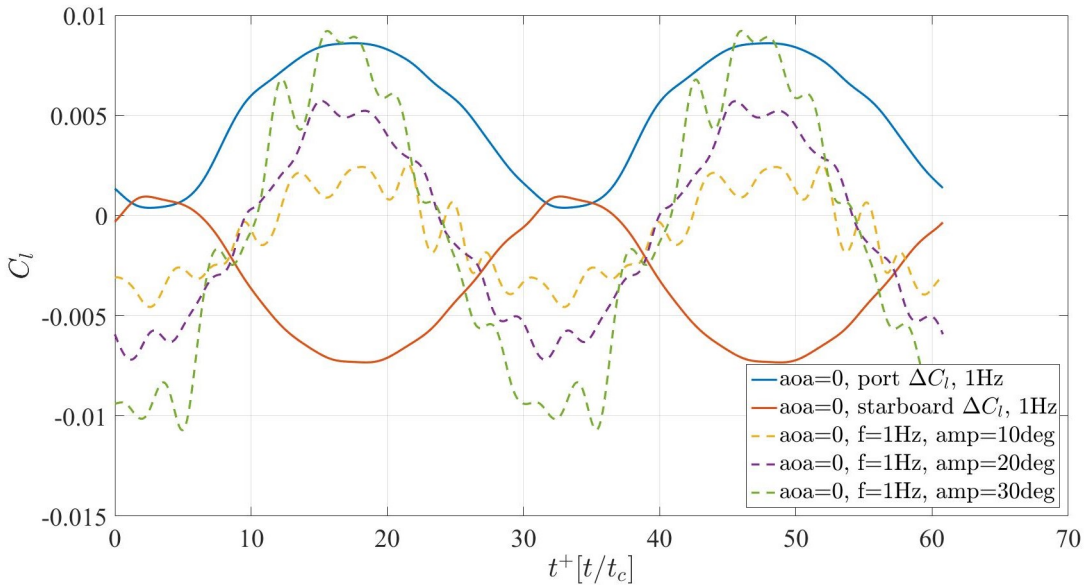

Figure 4.6. Control authority on roll moment coefficient at 1.0 Hz (AOA = 0°)

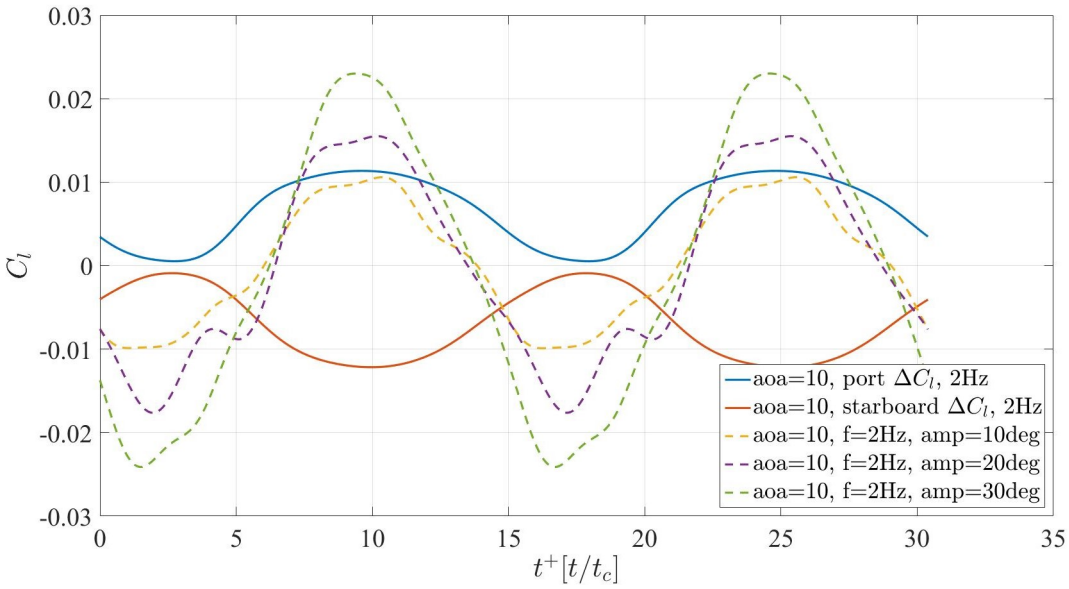

Figure 4.7. Control authority on roll moment coefficient at 2.0 Hz (AOA = 10°)

CHAPTER 5

DESIGN OF THE CONTROL SYSTEM

5.1 Open-Loop Control System

The open-loop control system for the roll moment contains a static gain for the actuation, a plant model, a feedforward loop, and a disturbance model for the roll moment. Figure 5.1 shows the elements and the structure of the system.

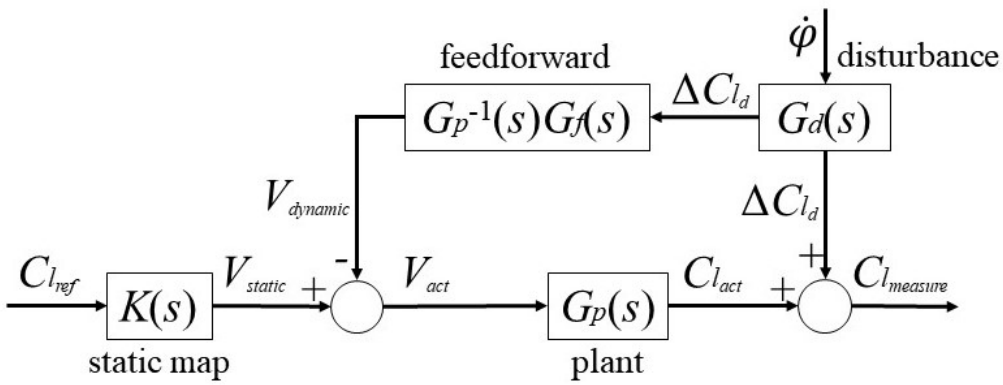

Figure 5.1. Block diagram of the control system for roll moment

In the control block diagram, $K(s)$ is the static gain which is obtained by inverting the static map of the actuation as discussed in Section 4.1.1. The quasi-steady response of the roll moment to the input voltage to the actuation is shown in Figure 5.2, in which the roll moment coefficient is the mean value of the hysteresis loop. The slope of the static map is 0.002 V^{-1}, thus the inversion of the slope give the static gain in the control loop, $K = 500$ V. When a particular reference roll moment coefficient Cl_{ref} is given as the input of the system, the static gain first converts Cl_{ref} to a voltage V_{static} that is required for the actuator input for the static actuation.

$G_p(s)$ represents the plant model that is used to predict the roll moment coefficient output from the dynamic actuation. As shown in the block diagram, the input of the plant model is the control voltage to the actuator V_{act}, the output, Cl_{act},

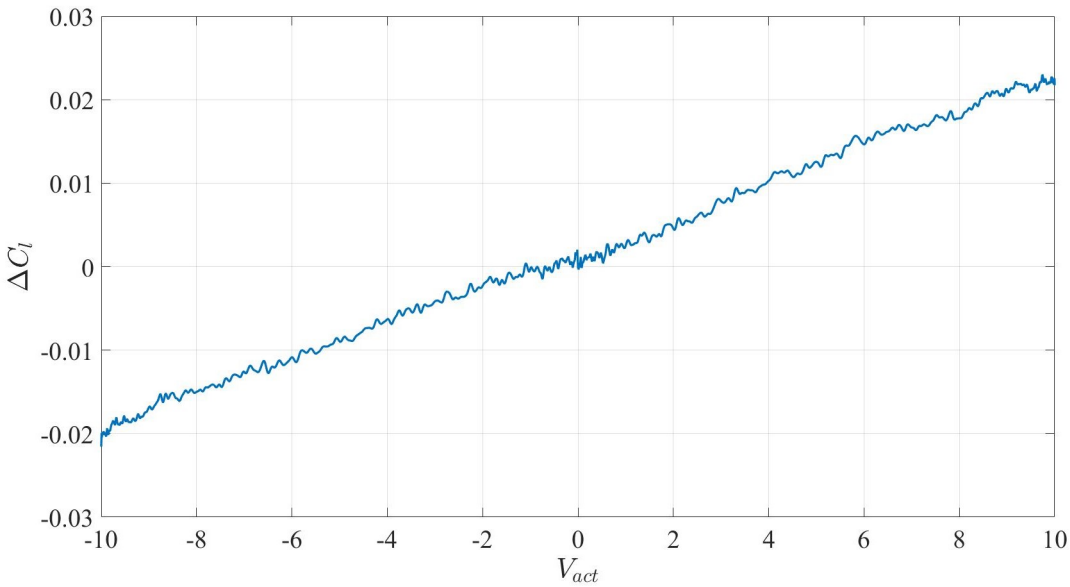

Figure 5.2. Static map of the roll moment coefficient response to the input voltage

is the predicted roll moment coefficient due to the actuation. The detailed modeling method of the plant is discussed in Section 5.2.

The disturbance model, $G_d(s)$, predicts the change of the roll moment coefficient, ΔC_{l_d}, that is caused by the roll motion. The relation between $\dot{\phi}$ and ΔC_{l_d} is identified to be utilized in the prediction. Thus, the roll rate is recognized as the disturbance input, and through the model, the change of the roll moment coefficient is obtained. The technique of identifying the disturbance model is discussed in Section 5.3.

The inversion of the plant model, $G_p^{-1}(s)$, and a low-pass filter, $G_f(s)$, construct the feedforward loop of the control system. The feedforward path uses the dynamics of the plant model to provide the system with an advance voltage input that compensates the influence of the disturbance on the system. The ΔC_{l_d} from the disturbance model is the input of the feedforward loop, and the output voltage, $V_{dynamic}$, is the response that is needed on the plant, which encounters the ΔC_{l_d} on

the system.

5.2 Plant Model

The identification of the plant uses pseudorandom binary signals (PRBS) as input to obtain the dynamic response of the actuators [16]. Based on the input voltage range of the actuators, the PRBS is modulated by 5 levels ($0-2$ V, $0-4$ V, $0-6$ V, $0-8$ V, $0-10$ V) of amplitude, respectively. For each amplitude level, the frequency of the PRBS varies from 0 to 2.0 Hz (exclude 0 Hz), so that the system identification covers the the full spectrum of the amplitude and frequency of the input signal.

Before the model identification, the PRBS input and output signals are normalized. At at certain angle of attack, third-order linear models are identified for the port (left) actuator and the starboard (right) actuator at each input amplitude, so that 10 models are identified for one angle of attack. Samples of the input and output measurements and the model prediction for one cycle of PRBS are shown in Figure 5.3. The high frequency signal is ignored in the identification.

This procedure is repeated for two angles of attack, $\alpha = 0°$ and $\alpha = 10°$. Therefore, 20 models are identified. Among all of the models, a nominal model is chosen to represent the family of models. Figure 5.4 shows the frequency responses of the models. Because the high frequency response is not of the concern of this thesis, the nominal model is only picked to handle the low frequency response.

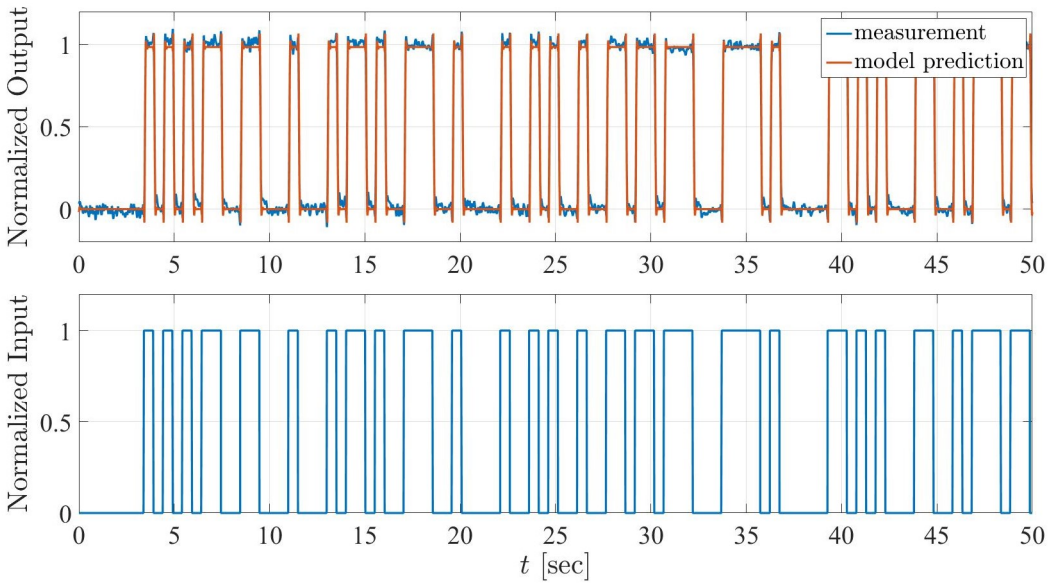

Figure 5.3. Sample of PRBS input and output signals and identified plant model output

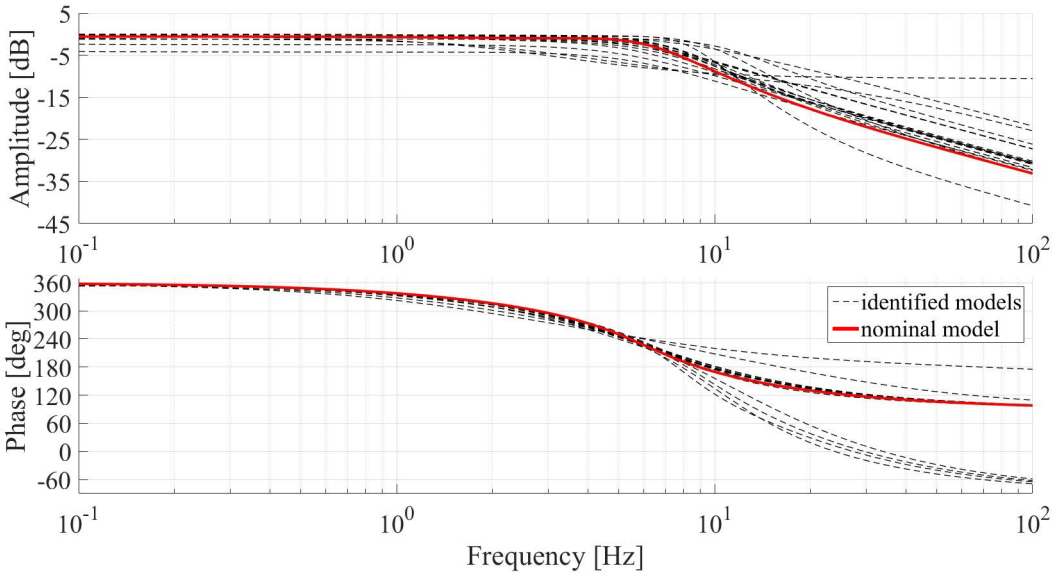

Figure 5.4. Frequency responses of the identified models and the nominal model

Since the nominal model is identified through the normalized input and output data, the plant model needs a family of gains to handle the magnitude of the dimensional inputs and outputs, as illustrated in Figure 5.5. For different input levels, the plant model gives corresponding output levels; the gain, as a piecewise linear function of the input level, corrects the normalized output level to the true roll moment coefficient. The example of the gain at $\alpha = 10°$ is shown in Figure 5.6. The break points are the values of the input amplitude levels that are used in the model identification process. The gain between two near break points is linearly interpolated.

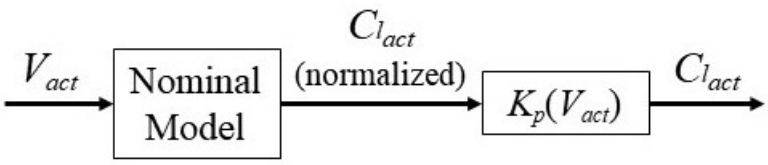

Figure 5.5. Nominal model and the plant gain

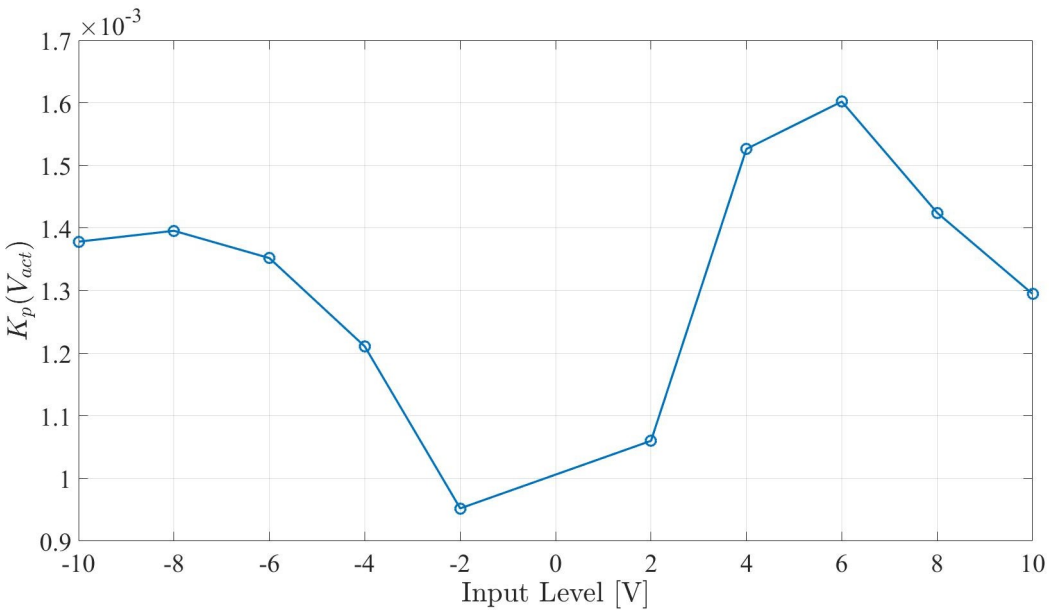

Figure 5.6. Function of the plant model gain at $\alpha = 10°$

5.3 Disturbance Model

As introduced in Section 5.1, the disturbance model is identified for the change of the roll moment in response to the roll rate input. From Section 3.3.1, the phase difference between the ΔC_l and the $\dot{\phi}$ and the magnitude of ΔC_l to $\dot{\phi}$ ratio have been measured for different roll frequencies at different angles of attack. The disturbance model is supposed to reproduce these responses on the frequency domain.

The disturbance models are identified for different angles of attack. At each angle of attack, the input and output data of different roll frequencies are transformed to the frequency domain to obtain a third-order model. Similar to the process of identifying the plant model, the model which matches the phase and magnitude measurement the most is determined as the nominal model for that angle of attack. The identification results are shown in Figure 5.7 to Figure 5.10. Again, the high frequency response is not taken into consideration, since the highest frequency of the roll rate is up to 2.0 Hz.

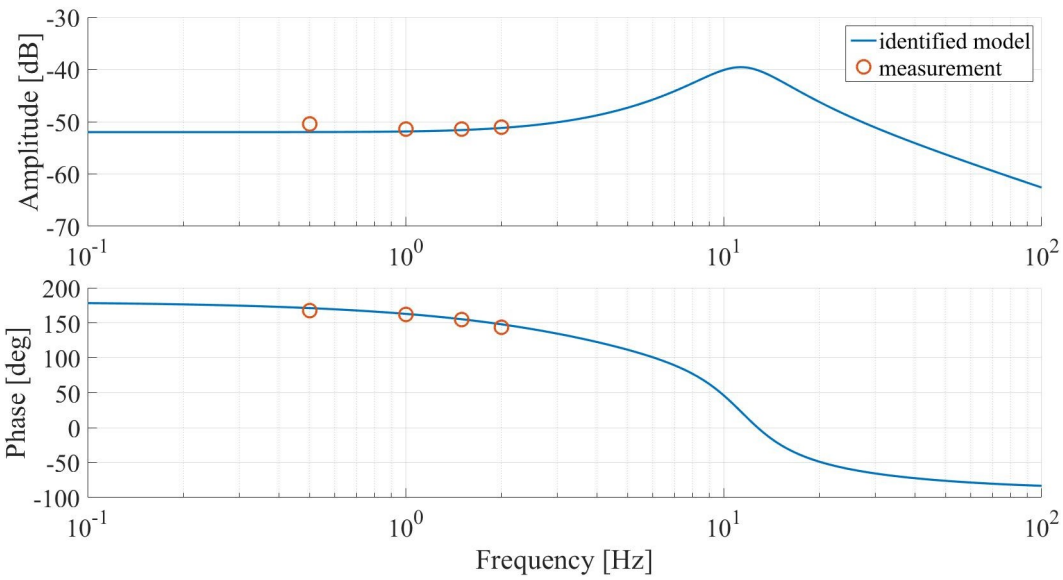

Figure 5.7. Frequency response of the disturbance model at $\alpha = 0°$

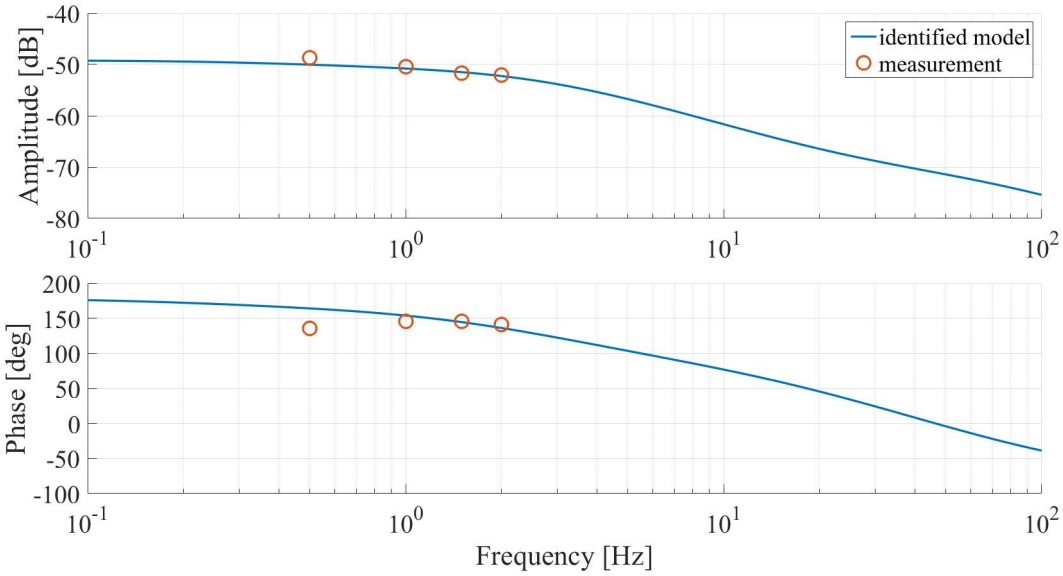

Figure 5.8. Frequency response of the disturbance model at $\alpha = 5°$

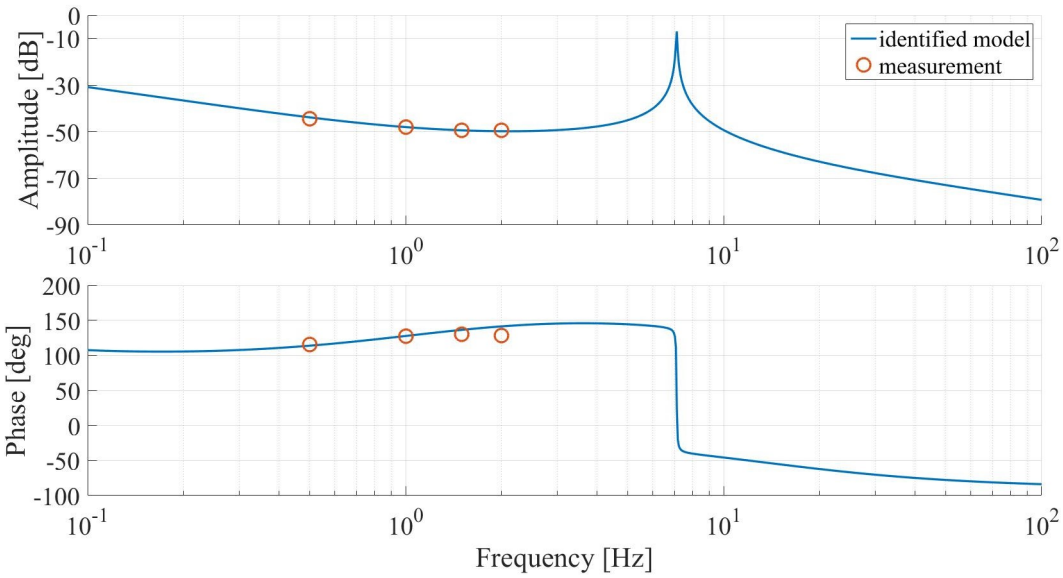

Figure 5.9. Frequency response of the disturbance model at $\alpha = 10°$

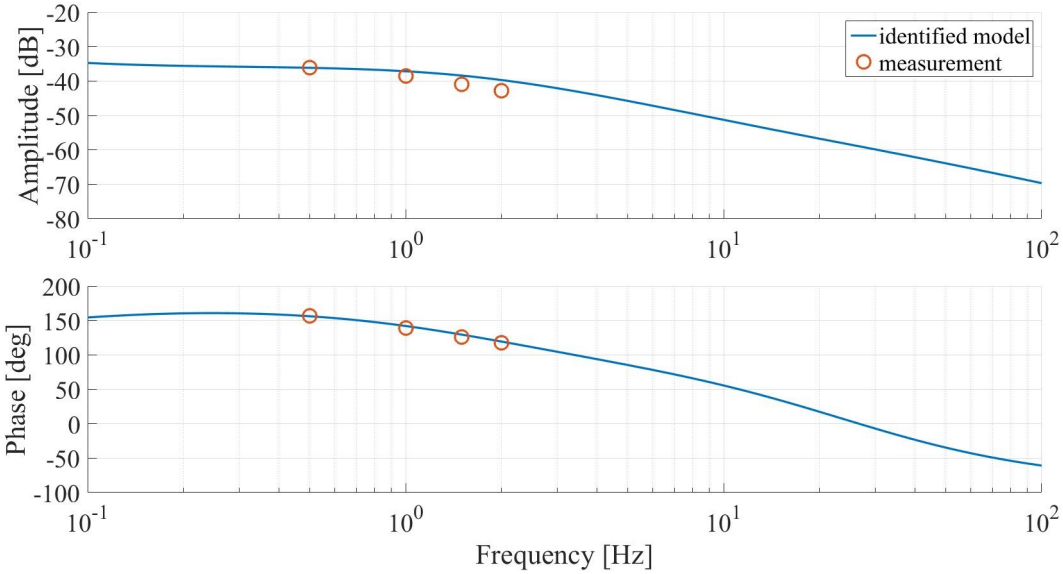

Figure 5.10. Frequency response of the disturbance model at $\alpha = 20°$

5.4 Simulation Results

5.4.1 Plant Model Simulation. Figure 5.11 and Figure 5.12 give two sample simulation results of the plant model at $\alpha = 0°$ and $\alpha = 10°$. In the diagrams, the x-axis is the instantaneous time in the simulation, and the y-axis is the roll moment coefficient. The yellow line and the blue line represent the simulation result and the experimental measurement respectively. In Figure 5.11, the actuation is on the port side and the actuation input frequency is 2.0 Hz. The example in Figure 5.12 shows the starboard actuation at 1.0 Hz.

The simulation results demonstrate that the plant model is able to capture the dynamics of the actuation correctly. With proper gain interpolations, the model also gives correct prediction on the magnitude at different angles of attack. In addition, the model has good sustainability for actuation on both sides at various actuation frequencies.

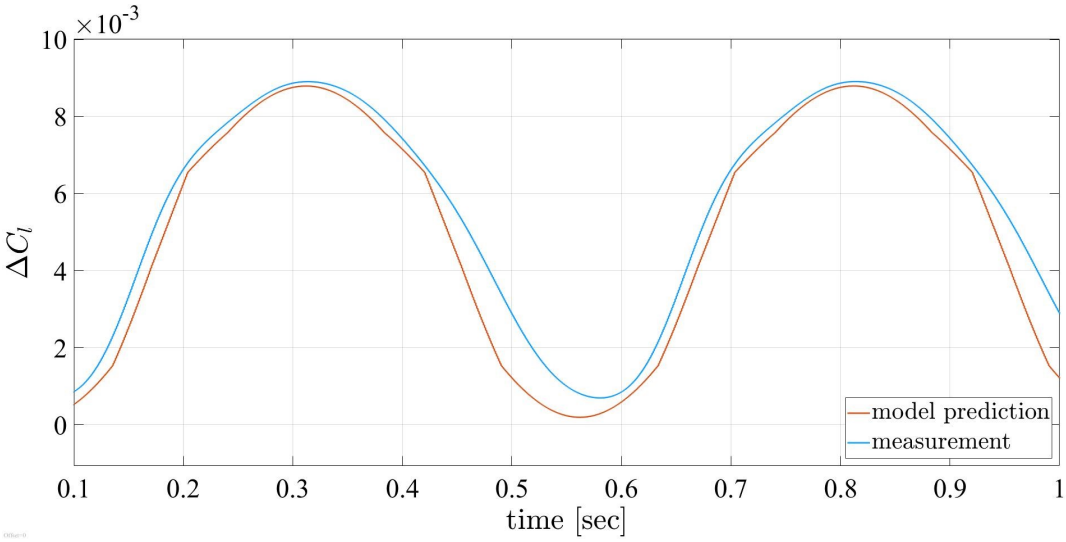

Figure 5.11. Simulation result of the plant model at $\alpha = 0°$

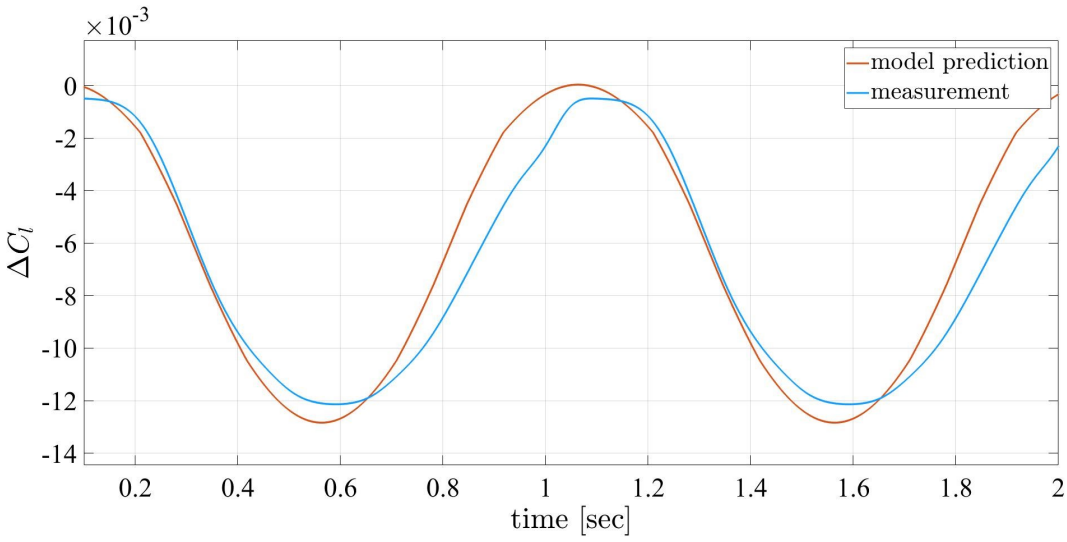

Figure 5.12. Simulation result of the plant model at $\alpha = 10°$

5.4.2 Inverted Plant Model Simulation. To test the capability of the feedforward loop, the measurement signals which are the reference signals in the simulation from Section 5.4.1 are used as the input signals to the inverted model. The output signal from the inverted model is compared with the input signal to the plant model, which is the true input voltage to the actuators. Therefore, the performance of the feedforward loop can be evaluated through the comparison.

Two example results which correspond to cases from in Section 5.4.1 are shown in Figure 5.13 and Figure 5.14. Except for the initial conditions, the inverted model is able to reproduce the dynamics and the magnitude relatively well. However, a phase delay exists between the model prediction and the correct reference signal. Depending on the frequency of the input signal, this phase delay results in a time delay on the feedforward signal which various from 0.1 s to 0.2 s

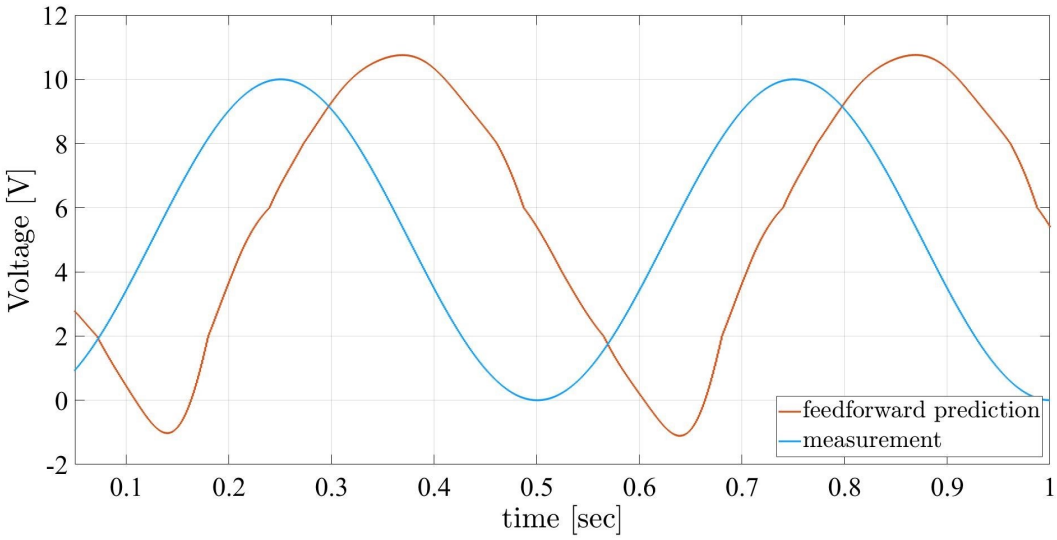

Figure 5.13. Simulation result of the feedforward loop at $\alpha = 0°$

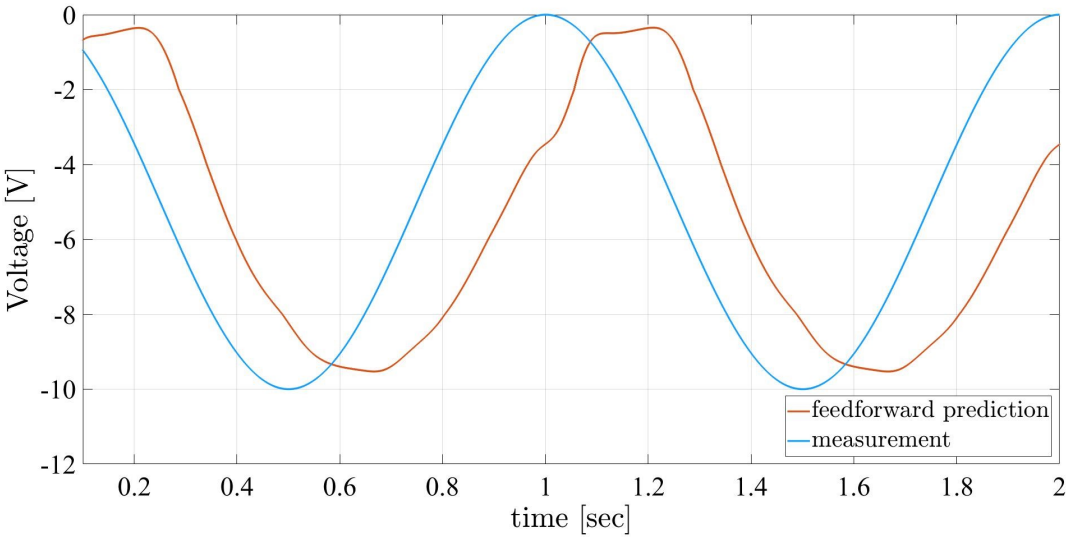

Figure 5.14. Simulation result of the feedforward loop at $\alpha = 10°$

5.4.3 Disturbance Model Simulation. Since the disturbance model is identified at each angle of attack, the simulation uses different nominal models for their corresponding angles of attack. Sample results of $\alpha = 0°$ and $\alpha = 20°$ with a same disturbance frequency (roll frequency) $f = 1.0$ Hz are shown in Figure 5.15 and Figure 5.16.

The simulation shows that each nominal disturbance model gives accurate prediction on ΔC_l at its applicable angle of attack. Especially, at high angle of attack, the model is more precise since the high frequency response to the disturbance is not as sensitive as it is at low angle of attack.

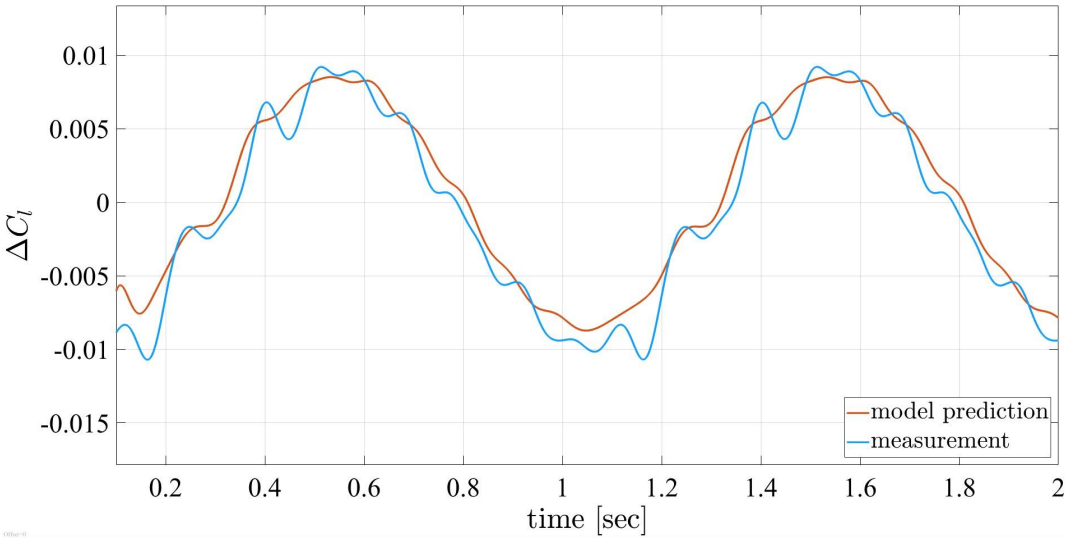

Figure 5.15. Simulation result of the disturbance model at $\alpha = 0°$

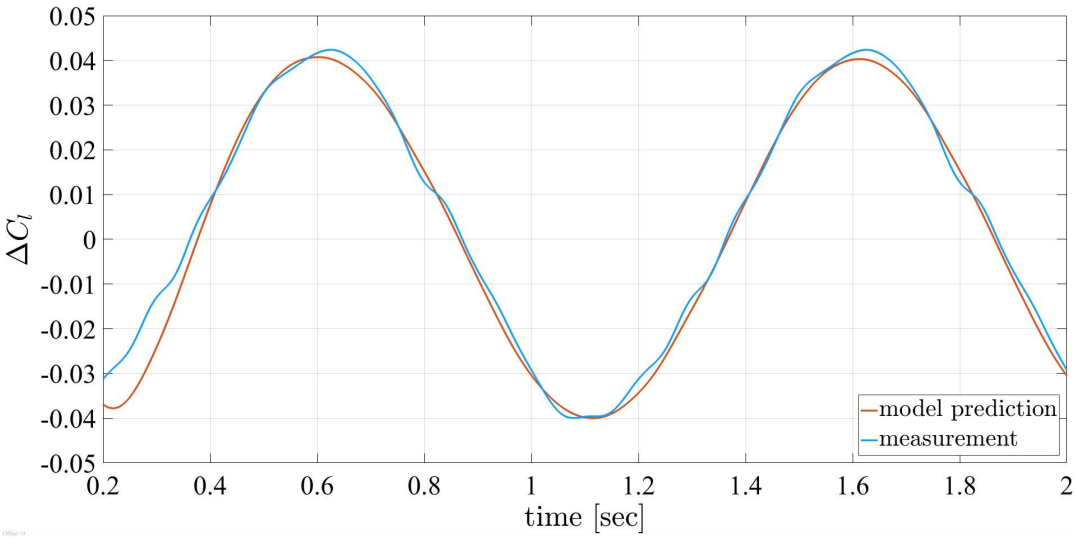

Figure 5.16. Simulation result of the disturbance model at $\alpha = 20°$

5.4.4 Open-Loop Control Simulation. As discussed in Section 5.1, the static map, the plant, the feedforward loop, and the disturbance model make up an open-loop control system for the roll moment coefficient. Based on the control block diagram in Figure 5.1, the open-loop controller is developed in Simulink® as shown in Figure 5.17.

Each component in the control system is specified with its corresponding model. The input to the system $C_{l_{ref}}$ is an artificial constant, about which the system is supposed to maintain the roll moment coefficient. Similar to the simulation of the disturbance model, the disturbance input to the whole system is a time series data of roll rate at a certain angle of attack, to which the disturbance model and the plant model gain correspond. At the output port, the non-controlled experimental measurement of the roll moment coefficient with the same roll rate and angle of attack makes the comparison with the controlled output.

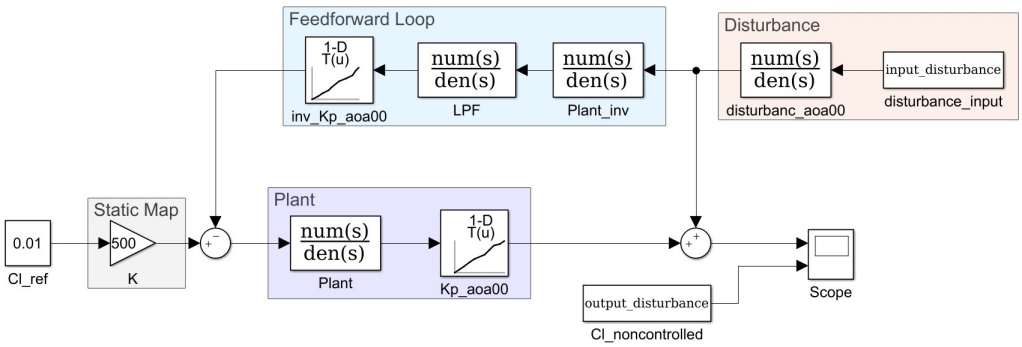

Figure 5.17. Simulink® diagram of the open-loop controller

The control objective is to to maintain a constant roll moment coefficient when the wing is undergoing the disturbance from the change of roll rate, which causes the roll moment to fluctuate. Examples of the controlled output at $\alpha = 0°$ are shown in Figure 5.18 ($C_{l_{ref}} = 0$) and Figure 5.19 ($C_{l_{ref}} = 0.01$). Despite the oscillation at the initial condition, the system is able to keep the roll moment coefficient fluctuating

within a significant smaller range than that of the non-controlled measurement. Furthermore, the system is able to shift the mean value of the output according to the $C_{l_{ref}}$ input.

If comparing the controlled and non-controlled results with respect to the roll angle, as shown in Figure 5.20, the capability of the controller to compensate for the roll moment is very apparent that the hysteresis loop of the aerodynamic roll moment has greatly diminished under the control.

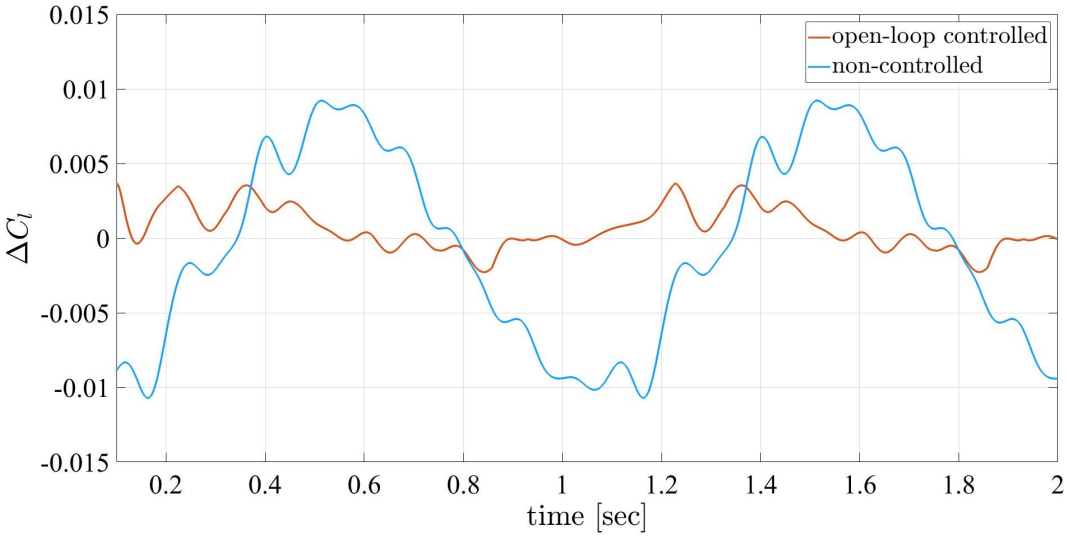

Figure 5.18. Simulation result of the open-loop controller with $C_{l_{ref}} = 0$

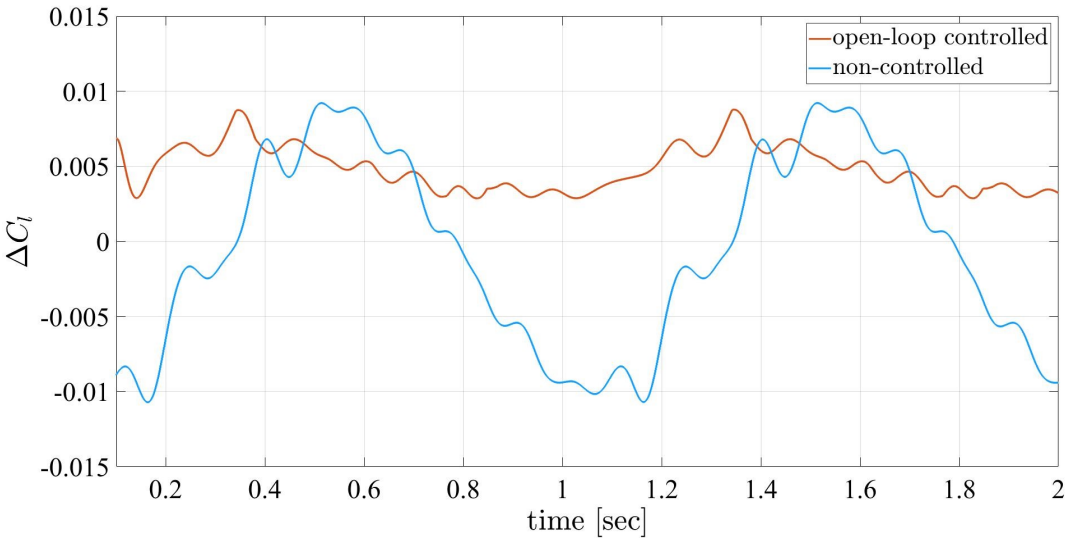

Figure 5.19. Simulation result of the open-loop controller with $C_{l_{ref}} = 0.01$

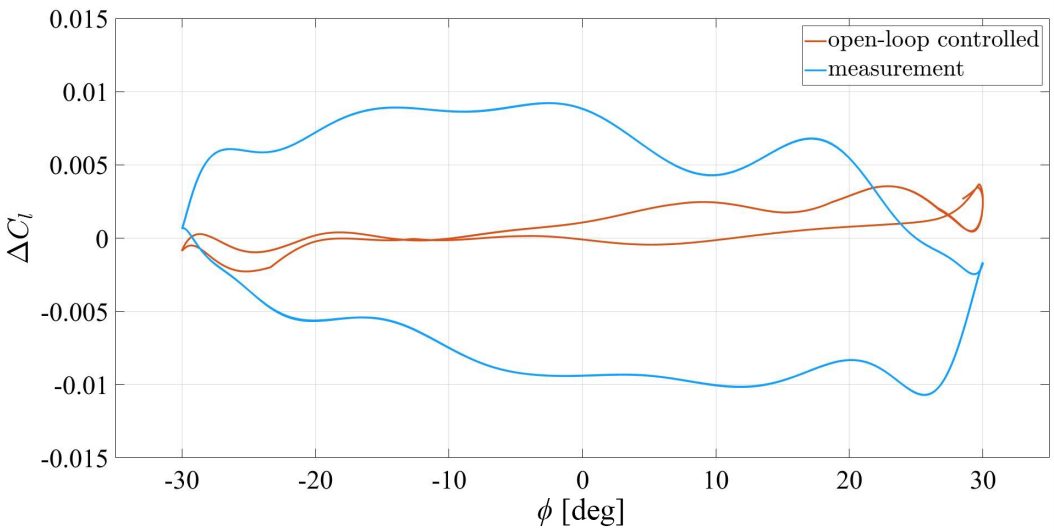

Figure 5.20. Simulation result of attenuation of the roll moment hysteresis loop

CHAPTER 6
CONCLUSION

6.1 Summary of the Aerodynamic Force and Pressure Measurements

This thesis conducts experiments to measure the steady and dynamic aerodynamic forces and moments as well as the surface pressure on a UCAS delta wing in dynamic roll motion. The dynamic roll moment behavior is found to be highly affected by the roll rate (or reduced frequency) and the angle of attack. The roll motion also causes a coupling between the roll and pitch moment, and this coupling largely depends on the angle of attack as well. The surface pressure measurements suggest diverse patterns of pressure change on the outboard wing and the inboard wing, which is considered to be connected to the leading edge vortex formation on the delta wing.

In the analysis of the roll moment, despite the proportional influence from the reduced frequency, the amplitude of the dynamic roll moment appears to be significantly dominated by the angle of attack when the wing moves from moderate angle of attack to high angle of attack. Jumps in the roll moment amplitude are found in every reduced frequency. On the other hand, the reduced frequency and the angle of attack also affect the phase delay between the roll moment and the roll rate. Unlike the amplitude, the phase delay does not show a uniform trend of change according to the roll rate or to the angle of attack.

The roll motion does not only change the roll moment, but also substantially affects the pitch moment as well as the lift in different ways at different angles of attack. Especially, the effect on shifting the mean value of the pitch moment at small angle of attack is highly sensitive to the change of the incidence.

The amplitude and phase delay characteristics of the roll moment as well as the

roll-pitch coupling phenomenon suggest that the aerodynamic forces and moments on a dynamic rolling delta wing are highly nonlinear with respect to the change of the roll rate and the angle of attack. The underlying aerodynamics needs to be further investigated.

6.2 Summary of the Actuation Tests and Open-Loop Control System

A pair of trailing edge pneumatic actuators are designed and tested for the purpose of controlling the roll moment on the wing through active flow control. The steady and dynamic measurements of the actuation first prove that there is sufficient control authority on the roll moment from the actuation. In the meantime, these measurements also give the basis for the static map and dynamic response of the actuation that are needed in the design of the open-loop control system.

Given the nonlinear characteristics of the roll moment, linear approaches are utilized to identify lower-order models for the plant and the disturbance of the control system. However, due to the nonlinearity of the roll moment responses to the disturbance and the actuation, separated disturbance models and plant gains have to be identified for different angles of attack. This is considered to be the major limitation of the linear approach at current stage.

Nevertheless, the simulation of the complete open-loop controller gives encouraging results about attenuating the the fluctuation of roll moment due to the disturbance from the roll rate. The controller is also able to maintain a certain value of the roll moment coefficient that is within the control authority of the actuation.

6.3 Future Work

The fundamental aerodynamics of the rolling delta wing is going to be investigated through finer measurements on the forces and surface pressure, as well as improved flow visualization techniques. Based on the understanding of the dynam-

ics of the roll moment, more precise linear models or nonlinear models should be developed for the actuation and disturbance.

While keeping studying the effect of the roll motion on the wing, pitch motion will be added to the experiments to further approach the true unsteady flying status of a UCAV.

For the control system, real time tests of the controller will be conducted to determine the performance of the open-loop control. On top of this, a feedback loop is going to be added to the system to close the loop. A model of the relation between the limited surface pressure measurements and the aerodynamic forces needs to be developed in order to build the feedback loop.

APPENDIX A

TYPICAL PERFORMANCE OF CLIPPARD EVP PROPORTIONAL VALVES

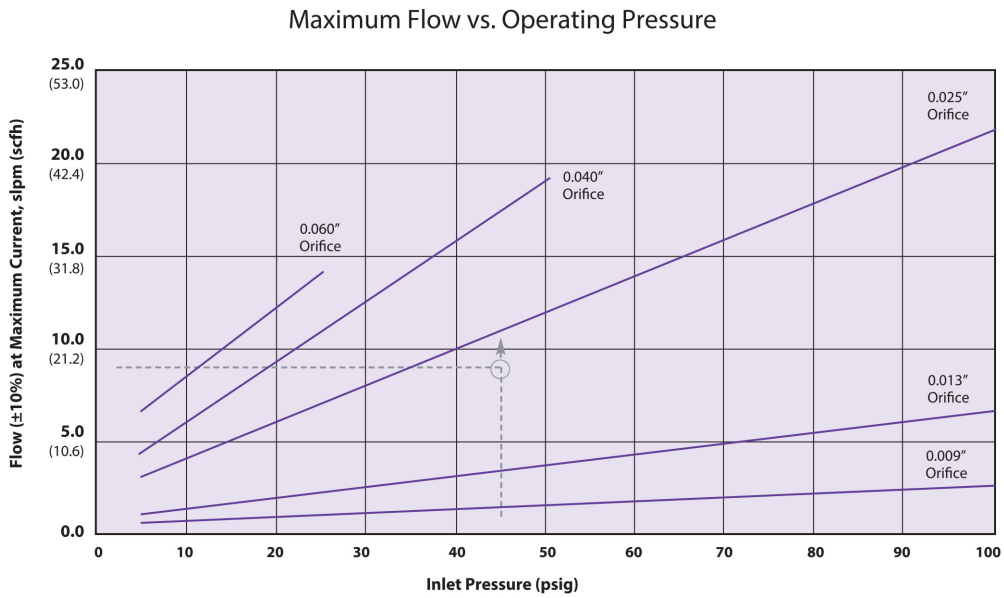

To determine the correct orifice required, locate the colored line immediately above the flow/pressure intersection
Example: 9 slpm required at 45 psig inlet. This example leads to a "-2545" valve (0.025" nozzle, 45 psig).

Figure A.1. Mass flow rate lookup chart of Clippard EVP Proportional Valves

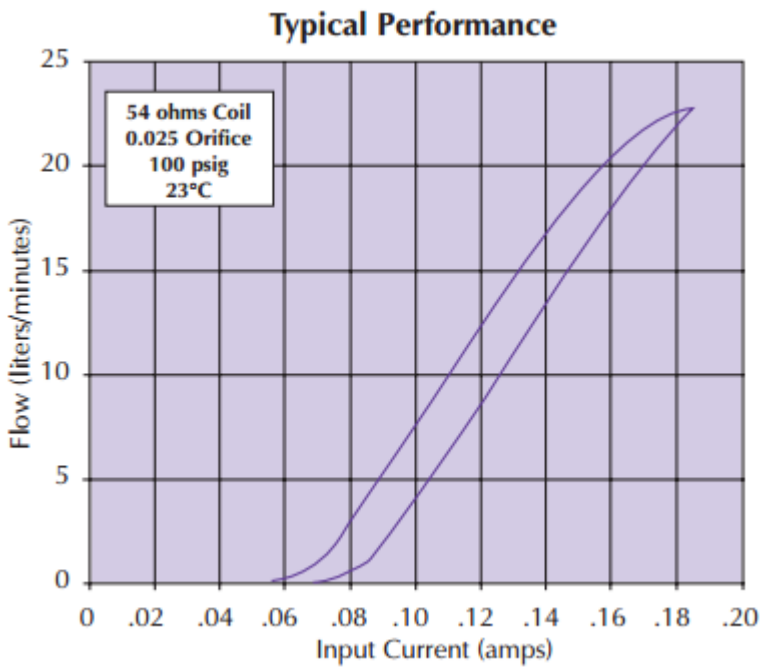

Figure A.2. Typical performance of Clippard EVP Proportional Valves

APPENDIX B

LIFT AND DRAG COEFFICIENT MEASUREMENTS OF THE ICE WING MODEL BY THE UNITIED STATES AIR FORCE ACADEMY

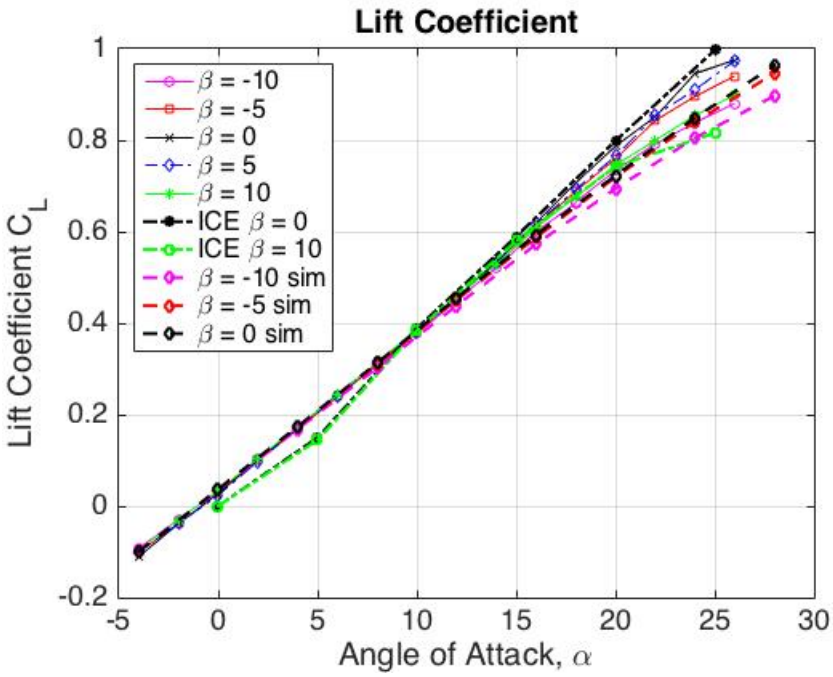

Figure B.1. Lift coefficient baseline of the ICE model

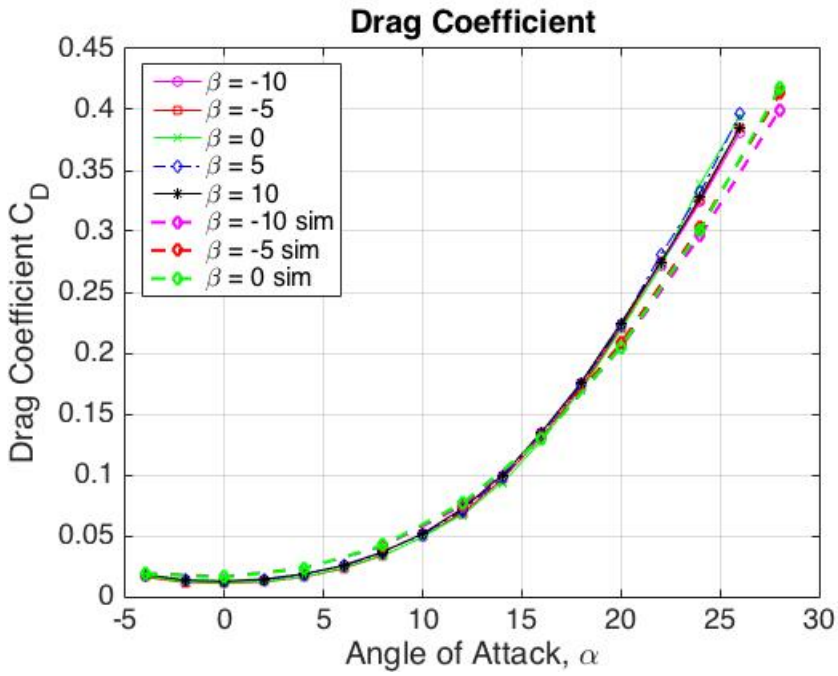

Figure B.2. Drag coefficient baseline of the ICE model

BIBLIOGRAPHY

[1] Clark, R. M. *Uninhabited Combat Aerial Vehicles: agirpower by the people, for the people, but not with the people.* Air Univ Maxwell AFB AL School of Advanced Airpower Studies, 1999.

[2] Luckring, J. M., and Boelens, O. J. "A reduced-complexity investigation of blunt leading-edge separation motivated by UCAV aerodynamics." *AIAA Science and Technology Forum and Exposition (SciTech 2015), AIAA Paper.* Vol. 61. 2015.

[3] Cherry, B. E., and Constantino, M. M. *The burble effect: superstructure and flight deck effects on carrier air wake.* Naval Academy Annapolis MD, 2010.

[4] Payne, F. M., Ng, T. T., Nelson, R. C., and Schiff, L. B. "Visualization and wake surveys of vortical flow over a delta wing." *AIAA Journal* 26.2 (1988): 137-143.

[5] Honkan, A., and Andreopoulos, J. "Instantaneous three-dimensional vorticity measurements in vortical flow over a delta wing." *AIAA Journal* 35.10 (1997): 1612-1620.

[6] Donohoe, S. R., and Bannink, W. J. "Surface reflective visualizations of shock-wave/vortex interactions above a delta wing." *AIAA Journal* 35.10 (1997): 1568-1573.

[7] Chaderjian, N. M., and Schiff, L. B. "Numerical simulation of forced and free-to-roll delta-wing motions." *Journal of Aircraft* 33.1 (1996): 93-99.

[8] Gad-el-Hak, M., and Ho, C. "The pitching delta wing." *AIAA Journal* 23.11 (1985): 1660-1665.

[9] LeMay, S. P., Batill, S. M., and Nelson, R. C. "Vortex dynamics on a pitching delta wing." *Journal of Aircraft* 27.2 (1990): 131-138.

[10] Gordnier, R. E., and Visbal, M. R. "Numerical simulation of delta-wing roll." *Aerospace Science and Technology* 2.6 (1998): 347-357.

[11] Gursul, I. "Unsteady flow phenomena over delta wings at high angle of attack." *AIAA Journal* 32.2 (1994): 225-231.

[12] Menke, M., and Gursul, I. "Unsteady nature of leading edge vortices." *Physics of Fluids* 9.10 (1997): 2960-2966.

[13] Gursul, I. "Review of unsteady vortex flows over slender delta wings." *Journal of Aircraft* 42.2 (2005): 299-319.

[14] Williams, D. R., An, X., Iliev, S., King, R., and Reißner, F. "Dynamic hysteresis control of lift on a pitching wing." *Experiments in Fluids* 56.5 (2015): 112.

[15] Margalit, S., Greenblatt, D., Seifert, A., and Wygnanski, I. "Delta wing stall and roll control using segmented piezoelectric fluidic actuators." *Journal of Aircraft* 42.3 (2005): 698-709.

[16] Kerstens, W., Pfeiffer, J., Williams, D. R., King, R., and Colonius, T. "Closed-loop control of lift for longitudinal gust suppression at low Reynolds numbers." *AIAA Journal* 49.8 (2011): 1721-1728.

[17] An, X., Grimaud, L., and Williams, D. R. "Feedforward control of lift hysteresis during periodic and random pitching maneuvers." *Active Flow and Combustion Control 2014*. Springer, Cham, 2015. 55-69.

[18] Sears, W. R., "Some Aspects of Non-Stationary Airfoil Theory and Its Practical Application." *Journal of the Aeronautical Sciences*8.3(1941): 104-108.

[19] Cook, M. V. *Flight dynamics principles: a linear systems approach to aircraft stability and control*. Butterworth-Heinemann, 2012. 20-21.

[20] Taylor, G., Wang, Z., Vardaki, E., and Gursul, I. "Lift enhancement over flexible nonslender delta wings." *AIAA Journal* 45.12 (2007): 2979-2993.